Miner Deposita (2016) 51:749–780
DOI 10.1007/s00126-015-0634-8

ARTICLE

A salt diapir-related Mississippi Valley-type deposit: the Bou Jaber Pb-Zn-Ba-F deposit, Tunisia: fluid inclusion and isotope study

Salah Bouhlel[1] · David L. Leach[2] · Craig A. Johnson[3] · Erin Marsh[3] · Sihem Salmi-Laouar[4] · David A. Banks[5]

Received: 16 June 2015 / Accepted: 17 December 2015 / Published online: 25 January 2016

Abstract The Bou Jaber Ba-F-Pb-Zn deposit is located at the edge of the Bou Jaber Triassic salt diapir in the Tunisia Salt Diapir Province. The ores are unconformity and fault-controlled and occur as subvertical column-shaped bodies developed in dissolution-collapse breccias and in cavities within the Late Aptian platform carbonate rocks, which are covered unconformably by impermeable shales and marls of the Fahdene Formation (Late Albian–Cenomanian age). The host rock is hydrothermally altered to ankerite proximal to and within the ore bodies. Quartz, as fine-grained bipyramidal crystals, formed during hydrothermal alteration of the host rocks. The ore mineral assemblage is composed of barite, fluorite, sphalerite, and galena in decreasing abundance. The ore zones outline distinct depositional events: sphalerite-galena, barite-ankerite, and fluorite. Fluid inclusions, commonly oil-rich, have distinct fluid salinities and homogenization temperatures for each of these events: sphalerite-galena (17 to 24 wt% NaCl eq., and Th from 112 to 136 °C); ankerite-barite (11 to 17 wt% NaCl eq., and Th from 100 to 130 °C); fluorite (19 to 21 wt% NaCl eq., Th from 140 to 165 °C). The mean temperature of the ore fluids decreased from sphalerite (125 °C) to barite (115 °C) and increased during fluorite deposition (152 °C); then decreased to ~110 °C during late calcite precipitation. Laser ablation inductively coupled plasma mass spectrometry (LA-ICP-MS) analyses of fluid inclusions in fluorite are metal rich (hundreds to thousands ppm Pb, Zn, Cu, Fe) but the inclusions in barite are deficient in Pb, Zn, Cu, Fe. Inclusions in fluorite have Cl/Br and Na/Br ratios of several thousand, consistent with dissolution of halite while the inclusions analysed in barite have values lower than seawater which are indicative of a Br-enriched brine derived from evaporation plus a component of halite dissolution. The salinity of the barite-hosted fluid inclusions is less than obtained simply by the evaporation of seawater to halite saturation and requires a dilution of more than two times by meteoric water. The higher K/Na values in fluid inclusions from barite suggest that the brines interacted with K-rich rocks in the basement or siliciclastic sediments in the basin. Carbonate gangue minerals (ankerite and calcite) have $\delta^{13}C$ and $\delta^{18}O$ values that are close to the carbonate host rock and indicate fluid equilibrium between carbonate host rocks and hydrothermal brines. The $\delta^{34}S$ values for sphalerite and galena fall within a narrow range (1 to 10‰) with a bulk value of 7.5‰, indicating a homogeneous source of sulfur. The $\delta^{34}S$ values of barite are also relatively homogeneous (22‰), with 6‰ higher than the $\delta^{34}S$ of local and regional Triassic evaporites (15‰). The latter are believed to be the source of sulfate. Temperature of deposition together with sulfur isotope data indicate that the reduced sulfur in sulfides was derived through thermochemical sulfate reduction of Triassic sulfate via hydrocarbons produced probably from Late Cretaceous source rocks. The $^{87}Sr/^{86}Sr$ ratio in the Bou Jaber barite (0.709821 to 0.711408) together with the lead isotope values of Bou Jaber galena ($^{206}Pb/^{204}Pb = 18.699$ to 18.737; $^{207}Pb/^{204}Pb = 15.635$ to 15.708 and $^{208}Pb/^{204}Pb = 38.321$ to 38.947) show that

Editorial handling: B. Lehmann

✉ Salah Bouhlel
salah.bouhlel@gmail.com

[1] Earth Sciences Department, Faculty of Sciences of Tunis, UR11ES16, University of Tunis el Manar, Tunis 2092, Tunisia

[2] Department of Geology and Geological Engineering, Colorado School of Mines, Golden, CO 80401, USA

[3] US Geological Survey, Denver, CO 80225, USA

[4] University of Badji Mokhtar Annaba, Annaba 23000, Algeria

[5] School of Earth and Environment, University of Leeds, Leeds LS2 9JT, UK

metals were extracted from homogeneous crustal source(s). The tectonic setting of the Bou Jaber ore deposit, the carbonate nature of the host rocks, the epigenetic style of the mineralization and the mineral associations, together with sulfur and oxygen isotope data and fluid inclusion data show that the Bou Jaber lead-zinc mineralization has the major characteristics of a salt diapir-related Mississippi Valley-type (MVT) deposit with superimposed events of fluorite and of barite deposition. Field relations are consistent with mineral deposition during the Eocene–Miocene Alpine orogeny from multiple hydrothermal events: (1) Zn-Pb sulfides formed by mixing of two fluids: one fluid metal-rich but reduced sulfur-poor and a second fluid reduced sulfur-rich; (2) barite precipitation involved the influx of a meteoric water component that mixed with a barium-rich fluid; and (3) fluorite precipitated from a highly saline fluid with higher temperatures.

Keywords Fluid inclusions · Laser ablation ICP-MS · C, O, S, Sr, Pb isotopes · Diapir-related MVT Ba-F-Pb-Zn deposit · Bou Jaber · Tunisia

Introduction

Lead-zinc ore deposits associated with salt halokinesis (salt tectonics) and evaporite diapirism are well known and have been exploited for many years in North Africa and the Gulf of Mexico of the USA (Hanna and Wolf 1934; Sainfeld 1956; Price and Kyle 1983; Light et al. 1987; Posey and Kyle 1988; Kyle and Posey 1991; Posey et al. 1994). They form a distinct group within the Mississippi Valley-type (MVT) class of deposits, with typically low to high tonnage and modest to high grade (Leach et al. 2005).

North Tunisia and the adjacent Algeria region host numerous Pb-Zn (±Ba-F) deposits located at the edges of Triassic salt-bearing diapirs. These deposits were exhaustively investigated and explored during the last eight decades, but important metallogenic aspects remain a subject of debate. Conflicting genetic models involving syngenetic origin, epigenetic origin, or a combination of both have been proposed (e.g., Sainfeld 1956; Rouvier et al. 1985; Charef and Sheppard 1987; Orgeval 1994; Sheppard et al. 1996; Bouhlel 2005; Bouhlel et al. 2007, 2009).

The Bou Jaber Ba-F-Pb-Zn deposit is located in central-western Tunisia, 30 km west of Tajerouine city, and close to the Algerian-Tunisian international border (Fig. 1). Unlike most of the Tunisian-Algerian salt diapir-related Pb-Zn deposits, the Bou Jaber deposit is barite- and fluorite-rich and exhibits a clear spatial relationship with three geo-structural elements: (i) Triassic salt diapir; (ii) Late Aptian/Late Albian unconformity; and (iii) NW-trending faults limiting grabens active during Eocene–Miocene times, allowing a possible role of these three geological controls in its genesis.

Currently no comprehensive geochemical investigation has been published on Bou Jaber. Based on mapping, general mineralogical descriptions and limited geochemical data the controversy over the genesis of the deposit has mainly included: (i) a syngenetic origin that involved meteoric karstification followed by the deposition of base metals originating from reworking of continental heavy-metal-rich soil horizons during Lower Albian times (Fuchs 1973; Amouri 1989); and (ii) an epigenetic origin at Miocene time, that involved replacement of limestone and infilling of hydrothermal dissolution cavities and open fractures by undefined fluids and precipitation processes (Bouhlel 1987, 1993; Salmi-Laouar 2004; Salmi-Laouar et al. 2004). To better define ore controls, the mineralizing event (s), the nature, origin, and evolution of the hydrothermal fluids, metal and sulfur sources, and the processes that control metal precipitation, this study integrates geological-mineralogical data, fluid inclusion microthermometry, halogen analysis of fluid inclusions, as well as stable (C, O, S) and radiogenic (Sr, Pb) isotope analysis on mineral separates. The results provide new insights into the origin of the Bou Jaber ore deposit and, in a more general sense, into the metallogenesis of diapir-related carbonate-hosted Pb-Zn-Ba-F deposits.

Geological setting

The NE-SW trending Tethyan *Tunisia Salt Diapir Province* (TSDP) in the eastern North African Alpine and Atlassic chains (Fig. 1), about 30,000 km^2 (300 km long, 100 km wide) is one of the world's salt diapir provinces that exposes important number of salt structures. It contains about a hundred Triassic salt diapirs and salt sheets which intruded about 8 to 10-km-thick Jurassic to Cenozoic sedimentary cover rocks (Perthuisot 1978, 1981). The diapirs are distributed in the two structural domains of the central-north Tunisian Alpine/Atlas fold-and-thrust belts, the Tell thrust-belt and the Atlas foreland fold-belt. The Atlas foreland is characterized by NE-SW trending faults and large-scale folds of Mesozoic and Tertiary sedimentary rocks (Ben Ferjani et al. 1990; Mejri et al. 2006). The Tell thrust-belt is characterized by southeast-vergent Tellian nappes (Late Cretaceous–Eocene, alternating limestones and marls) capped by the Numidian nappe (Oligocene Flysch) (Rouvier 1977). In the Atlas foreland, most of the diapirs crop out in the core of SW-NE anticline structures (Alpine direction); these are often overturned to the southeast. Diapirs are typically 10 × 3 km long and 1 to 2 km in width, and are distributed along reactivated Hercynian NE-SW directed faults (Sainfeld 1956; Perthuisot 1978, 1981; Martinez and Truillet 1987; Chaari 2002; Belayouni et al. 2012). At Bou Jaber, the Triassic salt crops out along the surface expression of the El Alia–Tajerouine diapir-bearing fault (Fig. 1). In the Tell thrust-belt, Triassic salt occurs as irregular masses and sheets between the nappes and the

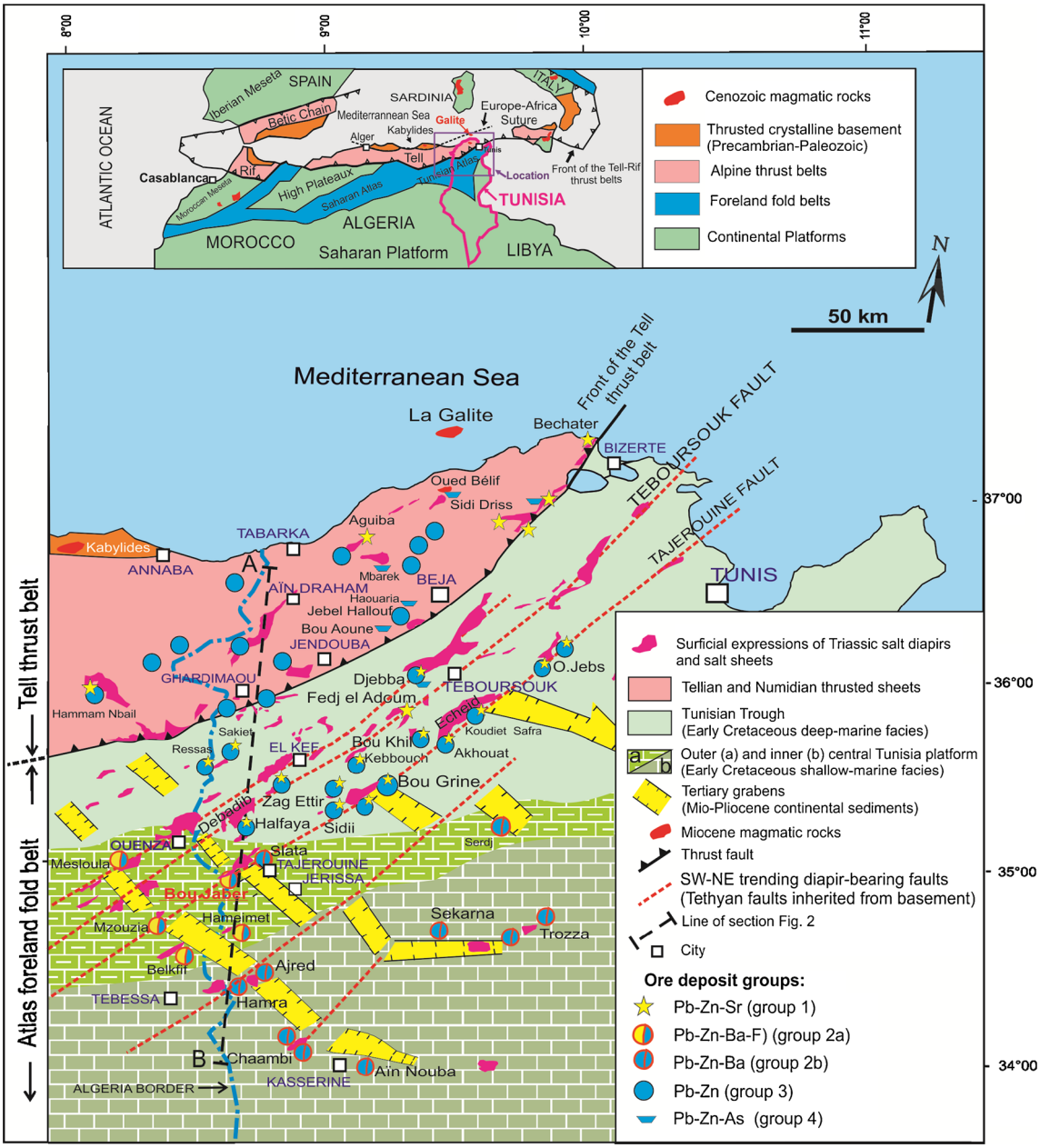

Fig. 1 Simplified structural and paleogeographic map of the TSDP showing the distribution of the Pb-Zn-Fe-Ba-Sr-F deposit groups discussed in text. Most of the ore deposits are spatially connected to Triassic structures (salt diapirs or salt sheets). Bou Jaber is located in the southwestern area of the province that corresponded to the transition zone between the Tunisian Trough and the southern central Tunisia platform. A-B line is cross section shown in Fig. 2. Regional location is shown on inset map

underlying autochthonous series. Triassic rocks were cut from the diapirs and stretched southward by the moving nappes or injected in faults through the nappes.

The Triassic salt has been severely folded and brecciated under the effect of halokinetic tectonic dissolution. Presently, it consists of chaotic anhydrite (often converted to gypsum)-rich megabreccias, referred here to as anhydrite cap rock which contains irregular blocks and masses of dolostone, variegated shales, and clays, as well as psammitic siltstone and minor altered tholeiitic basalt (ophite). At or near the surface, halite is partly or completely dissolved, but numerous saline springs indicate that salt is present at depth. Recent wells drilled through the diapirs encountered massive salt horizons about 200–300 m below anhydrite cap rock.

The Mesozoic–Cenozoic geodynamic evolution and the associated halokinetic salt tectonics of the north Tunisia margin, which formed during the rifting episodes of the Tethys ocean and its closure, are related to the convergence between

the Europe and Africa plates. This procession of geologic evolution may be described in successive tectono-sedimentary cycles as described below.

The Triassic rifting led to the formation of an epicontinental domain with vast subsiding evaporitic areas, where a ~1000-m-thick evaporite sequences of gypsum and halite (with silts, shales, clays, and shallow marine dolostone intercalations) unconformably overlies the Precambrian–Paleozoic basement (Ben Ferjani et al. 1990). During Middle Jurassic–Early Cretaceous times, intense rifting in the Tethys ocean produced in the northern Tunisia Tethyan passive margin two distinct paleogeographic and sedimentary domains, oriented ~SW-NE (Figs. 1 and 2), which include a subsiding furrow called the Tunisian Trough in the northwest and a central Tunisia carbonate platform in the south (Bolze et al. 1952; M'Rabet 1987; Vially et al. 1994; Bouaziz et al. 2002). In the Tunisian Trough, an as much as 5000-m-thick pelagic sequence, composed of shale-marl-clayey limestone alternations, was deposited during Middle Jurassic–Early Cretaceous times. On the platform, the thicknesses are reduced and gaps occurred. The lithofacies are composed of sandstone, clays, marls, and limestones (Marie et al. 1984; M'Rabet 1987).

During the Late Aptian–Early Albian tectonic event (Austrian event), Tethyan major SW-NE faults generated tilted block morphology of basins, with uplifts, grabens, and the emersion of large areas in the inner platform zone (Boltenhagen 1985; Martinez and Truillet 1987). This event was accompanied by two Triassic salt halokinesis and diapirism episodes (Late Aptian and Middle Albian; Perthuisot 1981). The Late Aptian halokinesis consisted of local salt pillowing which caused variations in thickness and facies of the Late Aptian sedimentary deposits (Perthuisot 1981). This process is particularly evident in the outer platform area (southern margin of the Tunisian Trough) where salt pillows created a swarm of shoals promoting the development of the reef complex of the Serdj Formation built by corals, algae, rudists and orbitolinae (e.g., Bou Jaber, Slata, Jerissa, and Ouenza; Dubourdieu 1956; Masse and Chikhi-Aouimer 1982; Perthuisot and Rouvier 1992; Bouhlel 1993; Perthuisot et al. 1998). The Middle Albian halokinesis and diapirism event was generalized throughout the Tunisian Trough and on its southern outer platform, as a regional reactivation of Hercynian SW-NE trending extensional faults which created space for the Triassic salt to rise and intrude

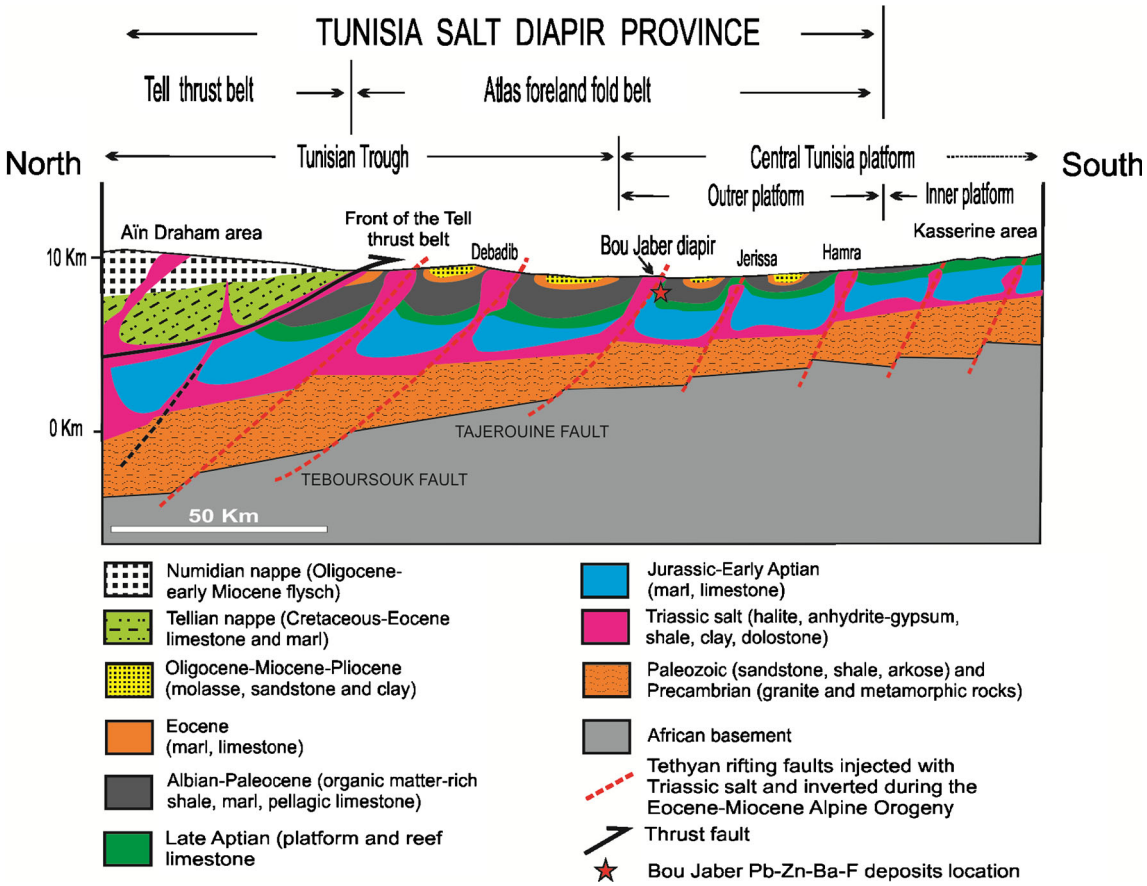

Fig. 2 Present-day interpretative N-S structural section of the Tunisia Salt Diapir Province (northern-central Tunisia), superposed on the main paleogeographic domains that prevailed during the Early Cretaceous times. Bou Jaber ores are located at the south side of a Triassic salt diapir. For location see A-B line in Fig. 1

the overlying units and extrude onto the seafloor (Bolze 1954; Perthuisot 1978, 1981; Bouhlel 1987, 1993; Vila et al. 1998, 1999; Vila and Charrière 1993; Chaari 2002; Belayouni et al. 2012).

The regional marine transgression of the post-rift stage started in the Late Albian and lasted till the end of the Paleocene and led to the deposition of a magasequence of pelagic to hemipelagic sediments. The lower part of this megasequence is composed of deep-water marine shale and marl (about 1000 to 1500-m-thick) called the Fahdene Formation (Late Albian–Cenomanian). It sealed structures related to the Late Aptian–Early Albian tectonics (uplifted Late Aptian shallow carbonate blocks and salt diapirs). The Fahdene Formation contains two black organic matter-rich and finely laminated limestone formations. These are the Late Albian sensu stricto Mouelha Formation (~2 wt% TOC) and the Late Cenomanian–Early Turonian Bahloul Formation (up to 13 wt% TOC) (e.g., Saïdi and Belayouni 1994; Soua 2009). These formations are believed to be the hydrocarbon source rocks for the Atlasic petroleum system (e.g., Saïdi and Belayouni 1994; Soua 2009). Following the Fahdene Formation is an about 2000-m-thick succession composed of marl-limestone alternations (Turonian–Paleocene).

Tectonic inversion of the north Tunisia Tethyan margin due to the subduction-collision of the European and African plates started during the Santonian (Cohen et al. 1980; Dewey et al. 1989; Guirand and Maurin 1991) and has generated complex structures and amplified the halokinetic and diapirism tectonics, through multiple compression and distension events. The first main compressional event occurred in the middle Eocene (Pyrenean; Castany 1952; Er-Raioui 1994; Tlig et al. 1991, 2010). It is characterized by WNW–ESE main regional stress (σ1) which led to moderate regional shortening that generated the SW–NE trending gently folded structures accompanied by emplacement of stacked thrust sheets (Tlig et al. 1991, 2010) and by the general emersion of most parts of Tunisia. It was during this time that most of the known diapirs of the TSDP where emplaced (Perthuisot 1981; Bouhlel 1987, 1993). Later on, a relaxation phase due to an Oligocene–early Miocene extensional event was accompanied by the deposition of about 600-m-thick continental clastic sediments (conglomerates, sandstones, and clays) supplied by the erosion of the reliefs related to the middle Eocene compressional structures. The middle Miocene phases (early Langhian and middle Tortonian) experienced compressional deformations that overprinted and amplified the Eocene SW–NE folds (Rouvier 1977; Turki et al. 1988). Diapiric structures were deformed and locally amplified. In areas where tectonic movements were more intense, Triassic diapirs were bent toward the SE in the Atlas foreland domain or disconnected and trailed under the nappes of the Tell domain. Thrust-faulting in the Tellian domain and in the more internal zone of the orogen (Kabylides and the La Galite Archipelago) generated multiphase calc-alkaline magmatism that intrudes the nappes during the Eocene (Tlig et al. 2010) and during the middle Miocene (Bellon 1976; Juteau et al. 1986; Laridhi-Ouazaa 1994) (e.g., granodiorite at the Nefza region and granite at the La Galite Archipelago). The post-orogenic relaxation phase on the Tell domain, in late Tortonian–Messinian times, produced molasses and lacustrine limestone deposited in the so called post-thrusting late Miocene basins (Rouvier 1977). NW–SE trending grabens in the Atlas foreland domain were due to the southeast directed greatest compressive stress (σ1) exerted during the middle Eocene, middle Miocene and Tortonian–Pliocene transpressional movements (Ben Ayed 1986; Philip et al. 1986; Chihi 1995). These grabens that intersect and cut across the SW–NE-oriented folds and Triassic diapir alignments were filled by Pliocene to Quaternary continental molasse and sandstone deposits.

Pb-Zn deposits and ore mineral assemblages

The main Pb-Zn ± (Ba, Sr, F) ore deposits of the TSDP are shown on Fig. 1. Each of these deposits contains low to medium size resources (1 to 8 Mt at about 5 to 15 % Pb + Zn). A number of important regional and local geological features controlled ore deposition in this province. Most of the ore deposits are distributed along parallel SW–NE trending faults, corresponding to reactivation of Hercynian faults during the Tethyan rifting, which were inverted during the Alpine Eocene–Miocene tectonics. The ore deposits are generally located at the southeast edges of the Triassic salt diapirs and especially at the NE and SW extremities of the diapirs. These mineralized zones correspond to areas where the diapiric structures intruded organic-rich marine strata and oil traps and are cut by NW-trending normal fault system limiting grabens active during late Eocene-late Miocene–Pliocene times. Most of the ores are linked to one of the following unconformities within the peridiapiric cover rocks: (i) Triassic/cover rocks, (ii) Late Aptian/Late Albian, and (iii) intra-Miocene unconformities. Most of the ore zones are located in carbonate traps showing abundance of oil seeps just beneath a seal of thick shale-rich formations. Thus, Triassic salt diapiric structures along SW–NE deep basement faults, intersection zones between Triassic salt diapirs and the NW-tending grabens, various unconformities in the peridiapiric cover rocks, and organic matter-rich strata, all played a role in controlling fluid circulation and ore precipitation.

The ore deposits can be classified into four groups based on the ore minerals present (Rouvier et al. 1985; Bouhlel 1993, 2005). The metal assemblages are not present in all deposits and where they do occur, they may or may not be present in specific mineralized zones. In all cases, where they occur in the same mineralized zone, there is a consistent paragenetic relationship, which is discussed later. These four groups may reflect complex hydrothermal overprinting by up to three

mineralization events in some deposits. The ore groups are briefly described below:

(1) Celestite ± (Pb-Zn) strata-bound replacement-type deposits within Triassic evaporite solution breccias (Transition zone) at the contact between salt diapirs or salt sheets and the surrounding Cretaceous to Miocene rocks (e.g., Fedj el Adoum, Kebbouch, Bou Khil, Guern Halfaya, Zag Ettir, Aguiba, Bechater). If Pb-Zn sulfides or barite are present in these deposits, they always cut the celestite ore bodies. The most economic deposit is Fedj el Adoum, containing about 1.5 Mt of 17 % Zn + Pb and little or no celestite (Sheppard et al. 1996; Bouhlel et al. 2007).

(2) Pb-Zn ± (Ba ± F) strata-bound replacement-type and cavity-filling deposits within Late Aptian carbonates covered unconformably by Late Albian–Cenomanian shale-rich formation at the edges of Triassic salt diapirs. Two subgroups with distinct mineral assemblages are observed: Group 2a with Ba-F ± (Pb-Zn) (e.g., Mesloula, Mzouzia, Belkfif deposits in Algeria; Akrour et al. 1991; and Bou Jaber—this paper—in Tunisia); and Group 2b with Ba ± (Pb-Zn) deposits (e.g., Slata, Hamra, Ajred, Trozza) (Bouhlel 1993; Jrad and Perthuisot 1995; Béjaoui et al. 2013). Furthermore, Ba ± (Pb-Zn) mineralization is also present within the Cenomanian–Turonian dolostone (e.g., Aïn Nouba) (Sainfeld 1956; Fuchs 1973); and even in early Eocene phosphorite rocks (e.g., Sekarna) (Garnit et al. 2012).

(3) Pb-Zn strata-bound replacement-type and vein-type deposits that lack Ba, Sr or F, hosted by Late Cretaceous organic-rich limestone that are intruded by Triassic salt diapirs (e.g., Bou Grine, Akhouat, O. Jebs; Schmidt 1999; Bouhlel et al. 2009; Béjaoui et al. 2013). The Bou Grine deposit, mined from 1992 to 2006, had a resource of about 7.3 Mt of ore grading 9.7 % Zn and 2.4 % Pb (Orgeval 1994; Schmidt 1999; Bouhlel et al. 2009).

(4) Clastic-dominated Pb-Zn ± As deposits within late Miocene–Pliocene continental sequences deposited in post-thrusting basins (e.g., Bou Aouane, Jebba, and Sidi Driss) (Rouvier et al. 1985; Decrée et al. 2008).

The Zn-Pb-Ba-Sr-F ores show five distinct mineral assemblages: (1) celestite (monomineralic); (2) Zn-Pb sulfides; (3) barite (±trace sphalerite and galena) and (4) fluorite with minor barite (±trace sphalerite and galena). These various mineral assemblages are suggestive of contributions from at least four distinct ore fluids and/or ore-forming events variably affected by the Triassic diapiric structures with the Bou Jaber deposit containing a mineral assemblage that reflects mineralization from a Zn-Pb event, a barite event and a late fluorite event as discussed below.

The Bou Jaber deposit

The Bou Jaber deposit was first mined for Pb-Ag by the Romans during the second to the fifth centuries. From the ninth to the seventeenth centuries, small and episodic mining activities continued by the Arabs, then from 1890 to 1950 by the French. The period 1972–2004 was the most recent intermittent mining activity by Tunisian state-owned mining companies focused on underground exploitation with a total production of about 50,000 t Pb + Zn, 0.5 Mt barite and minor quantities of fluorite. The production ceased at the end of 2004 due to economic difficulties. The remaining estimated reserves are about 8 Mt with a grade of 1.5 % Pb, 3.5 % Zn, 33 % $BaSO_4$, and 9 % CaF_2. Recently, European Industrial and Base Metal Limited company concluded negotiations with the Tunisian government and earned a 90 % right in the Bou Jaber mine concession, while 10 % are detained by the Office National des Mines (O.N.M.). Mining activities will restart in the next few years.

Geology

The Bou Jaber diapiric structure is located in the central-western part of the TSDP and crops out in the southwest segment of the SW-NE trending Tajerouine–El Alia diapir-bearing fault (Figs. 1 and 2). The Bou Jaber structure (Fig. 3a–c) is a 10-km-long; 1- to 2-km-wide SW–NE directed pericline surrounding the SW to SSE margin of the Triassic salt formation. The pericline is made up of uplifted Late Aptian carbonate bars that are subvertically dipping and in places overturned to the SE probably by the intrusive Triassic salt diapir.

The Triassic salt crops out as a complex and chaotic megabreccia clasts composed of anhydrite cap rock, where the anhydrite masses, with flowage textures, occur together with deformed variegated clay layers and irregular meter- to hundred-meter-sized blocks of dolostone. In this cap rock, as in others of the TSDP, most of anhydrite has been converted to gypsum and halite rocks were dissolved. The boundary between Triassic salt and adjacent Late Aptian carbonate strata is of tectonic origin. It likely originated during salt halokinetic and salt diapirism events.

The Late Aptian platform carbonate succession (300- to 500-m-thick), which corresponds to the Serdj Formation of Burollet (1956), is subdivided into seven units grouped in three members (Bouhlel 1987, 1993; Braham et al. 2002; Salmi-Laouar 2004) (Fig. 3a-c):

1. The lower member (50- to 300-m-thick) consists of three massive limestone units (units 1, 3, and 5) separated by marly-dominated units (units 2 and 4). The marly-dominated units consist of green to dark-green marls (Oyster and Orbitolina-rich) with numerous thin

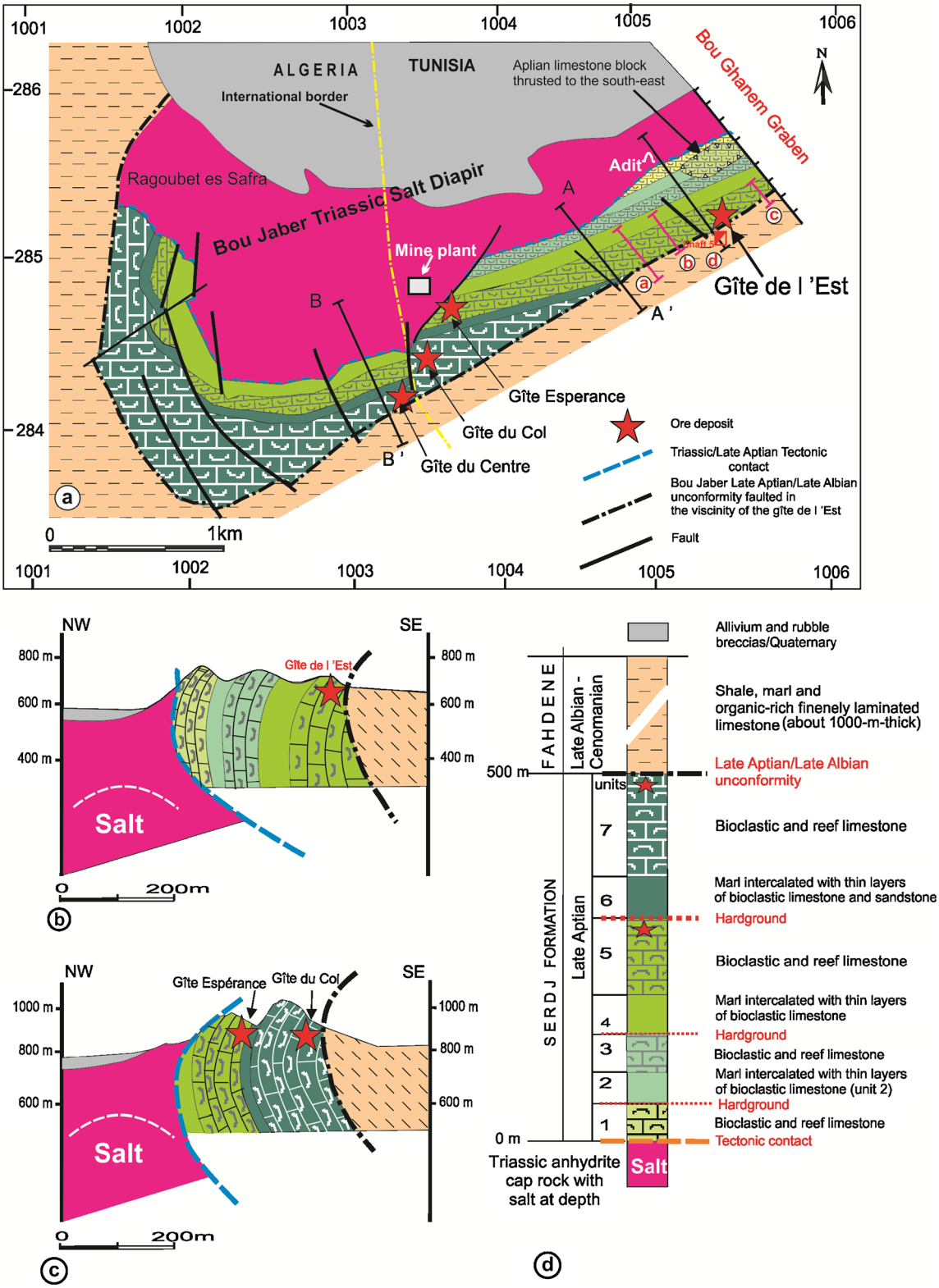

Fig. 3 **a** Geology map of the Bou Jaber Triassic salt diapiric structure showing stratigraphy, principal structural elements and the main F-Ba-Pb-Zn deposit locations, numbers are Lambert coordinates. **b** and **c** NW-SE cross sections located by the A-A' and B-B' lines respectively in figure a. **d** Stratigraphic column. Circled numbers a, b, c, d correspond to the cross sections a, b, c and d in Fig. 4

bioclastic limestone intercalations and rare siliclastic beds. The massive limestone units are made up of meter-thick bioclastic limestone rich in rudistids, corals, algae, and orbitolina debris in places intercalated by

biostromal facies dominantly formed by rudistids and coral colonies. The top of the unit 5 shows thin lithified and bioturbated and iron oxide-rich sediment layers characterizing hardground horizons.

2. The middle member (unit 6 on Fig. 3a–c) consists of an about 80-m-thick marl-dominated sequence containing thin layers of sandstone and bioclastic and orbitolina-rich intercalations.
3. The upper member (unit 7 on Fig. 3a–c) forms a lens-chapped bar of massive limestone thickening in map view from east to west from 50 to 250 m composed of bioclastic, reefal, and miliolidea-rich shallow marine facies. The top of this unit shows condensed 5- to 10-cm-thick sediment layers coated by iron oxides similar to hardground horizons found at the top of the unit 5. The Early Albian deposits, composed around the diapiric structure by about 300- to 500-m-thick deep marine marl sequences, are absent at Bou Jaber. This stratigraphic omission is related to post depositional erosion (Bouhlel 1987, 1993; Amouri 1989).

The Late Albian–Cenomanian shale-rich Fahdene Formation overlies with a weak angular unconformity from east to west the units 7 to 4 of the Late Aptian platform carbonate succession.

This spectacular cartographic discordance is materializing a major Late Aptian/Late Albian unconformity with a gap of the Early Albian sedimentation. The first transgressive layers of the Fahdene Formation forms a 0.2- to 1-m-thick horizon composed of dark marls containing siltstone, glauconite, phosphate, and debris flows of bioclastic limestone (ripped from the limestone below). Following is a 600-m-thick pelagic shale and marl succession containing at its lowermost part the Mouelha member (Late Albian sensu stricto) which is composed of about 10-m-thick organic-rich fine laminated limestone. On the top of the Fahdene Formation lies the Bahloul Formation that consists of about 20-m-thick organic-rich finely laminated limestone. Following is an about 2000-m-thick series of marl-limestone alternations of Turonian to Paleocene age.

The procession of geological evolution at the Bou Jaber from local and regional evidence may be described as follows. During the Late Aptian time, a salt pillow created a shoal on which a narrow platform with reef complex was developed promoting the accumulation of up to 500-m-thick Late Aptian shallow marine carbonates. The alternation of marly-dominated- and bioclastic to reef limestone units together with the presence of emersion features at the end of each of the reef limestone units are suggestive of continuous tectonic instability probably due to salt halokinesis pulses. Extensive drowning of the platform during the Early–Middle Albian time is interpreted by the facies change from carbonates to condensed phosphate-rich, terrigenous-influenced beds and emersion. At this time, the Bou Jaber salt diapir intruded its cover rocks. Similar salt intrusions have been observed in the neighboring diapiric structures (e.g., Jebel Slata; Perthuisot and Rouvier 1992; Perthuisot et al. 1998). The transgression and high sea level started during the Late Albian. This led to platform breakdown and to extensive pelagic and organic-rich sedimentation of the Fahdene shales and marls onto the platform area.

The Eocene northwest directed compression event was accompanied by renewal of diapirism. The Oligocene was a period of distension and continental erosion. The middle Miocene compression event amplified the halokinetic activities, overprinted the Eocene folds and overturned to the SE the diapiric structures. During these multiple tectonic events, the Late Aptian/Late Albian unconformity was overprinted and brecciated by the SW–NE-trending Bou Jaber fault. Numerous NW-SE to N-S trending faults cut the peridiapiric Late Aptian carbonate strata into a number of displaced blocks. The northeast termination of the Bou Jaber diapiric structure was intersected by NW-trending extensive normal faults limiting the Bou Ghanem graben.

Mineralization

The known Late Aptian carbonate-hosted mineralization at Bou Jaber forms several small to medium size deposits, which are fault and unconformity controlled and located at the southeastern flank of the northwest-dipping salt diapir. The deposits are dominated by barite or sphalerite + galena or fluorite: Pb + Zn + Ba at the *Gîte du col*; Pb-calcite at the *Gîte du Centre*; Pb-Zn + calcite at the *Gîte Espérance*; and Ba-F ± Pb-Zn at the *Gîte de l'Est* (Fig. 3a–c). This indicates that the western deposits are dominated by Pb-Zn and the eastern deposits are dominated by Ba-F (with minor Pb and Zn). Fluorite-rich zones are probably genetically related to the NW-trending faults limiting the Bou Ghanem graben.

The *Gîte de l'Est* mineralization (Fig. 4) is hosted within the limestone unit 5 of the Late Aptian carbonate which is unconformably overlain by the shale-rich Fahdene Formation. Mineralization occurs in brecciated limestone zones and in solution cavities and is distributed roughly along an E–W to SW–NE trending fault system parallel or overprinting the Late Aptian/Late Albian unconformity (Fig. 4a–c). Ore-rich zones are often located at the intersection zones of NE- and NW-trending faults. In the central part of the deposit, near shaft 5, rich ores form three roughly vertical ore bodies termed A, B, and C (Fig. 4d). Each of these has a thickness of 5 to 40 m, and is roughly E–W-striking, about 500- to 700 m long and extends to a depth greater than 400 m. Underground mapping and drill holes show that most ore bodies have the following zonation, from the border to the ore body core: sulfide-rich zone, mixed barite/sulfide zone, and late barite-rich zone.

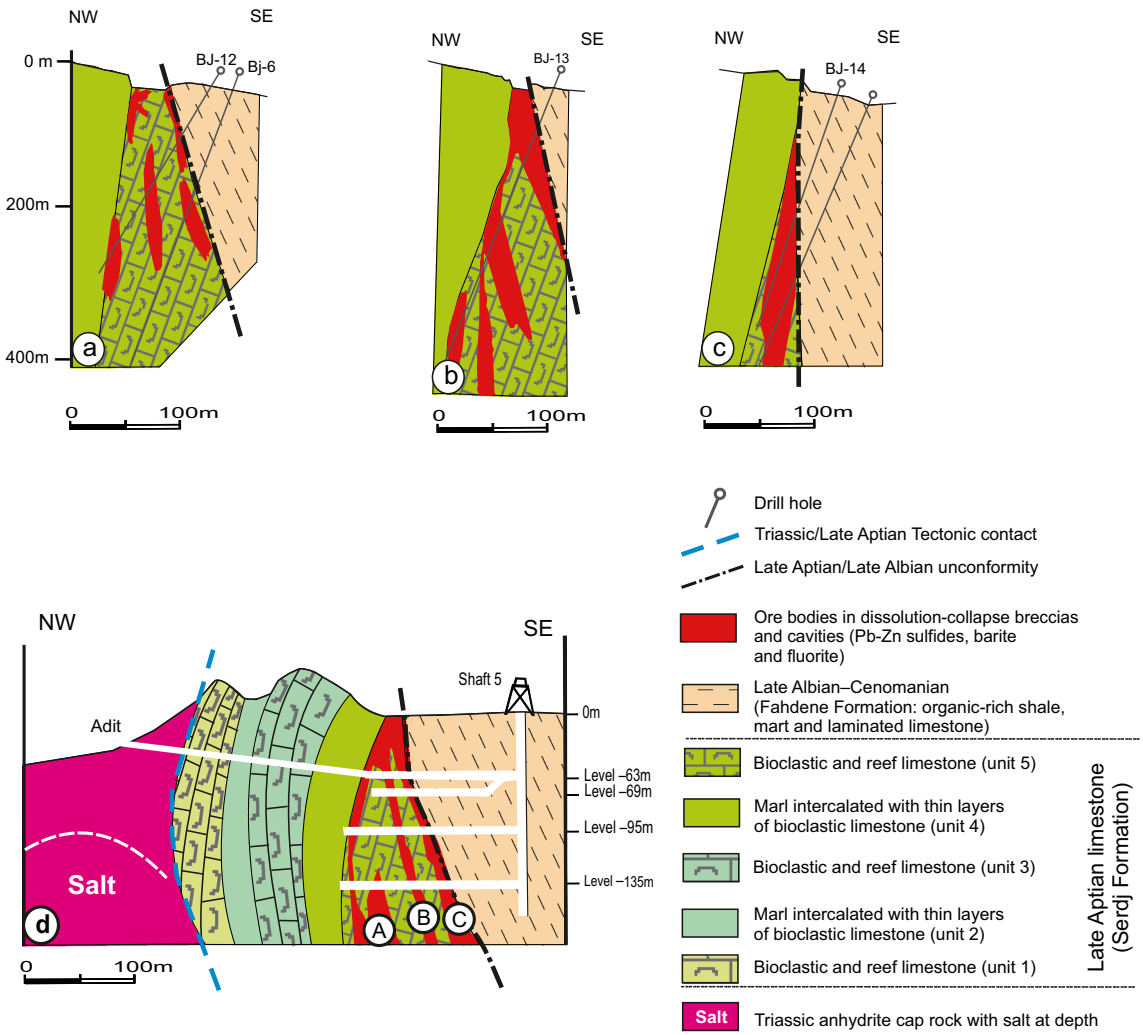

Fig. 4 NW-SE cross sections a, b, c, d of the Bou Jaber *Gîte de l'Est*, illustrated on the basis of field mapping in mining open pits, underground working exposures and drill holes. The sections show some of the vertical and lateral variations in volumes and morphologies of the dissolution cavities filled with the Pb-Zn-Ba-F ore crosscutting the Late Aptian limestone strata. In Fig. 4d, circled letters A, B and C indicate the main ore bodies of the *Gîte de l'Est* in shaft 5 area. For cross section locations see a, b, c and d lines in Fig. 3a

A number of liquid hydrocarbon seeps occur along fractures and within the permeable Late Aptian carbonate host rocks and as impregnations and residue within the ores. The hydrocarbons consist of saturated hydrocarbon (18.9 vol%), aromatic (7.2 vol%), asphaltene (55.6 vol%), and resin (18.3 vol%) (Maameri and Daadouch 1986). The total of the heavy hydrocarbon fraction is about 74 vol%, and the resin/asphaltene ratio is 0.34 (Maameri and Daadouch 1986). Potential source rocks belong to the Fahdene and Bahloul Formations containing ~2 wt% to ~13 wt% TOC, respectively (Saïdi and Belayouni 1994). These organic-rich formations were buried during the Campanian–Eocene period to a depth of about 3000 m, and organic maturation processes produced oil and gas as demonstrated by the numerous oil seeps in the Bou Jaber mine and neighboring regions and by oil wells sourced from the Late Aptian carbonates (e.g., Douleb and Semmama oil fields; Belayouni 1992). Oil generation probably began in the Campanian, resulting from subsidence, but peak petroleum generation probably occurred in Eocene and Miocene time (Belayouni 1992) in parallel with the Alpine orogenic events.

In the absence of direct dates on ore emplacement, constraints on the age of ore formation can be made from geological relationships. The ores are strongly controlled by various structural elements and therefore the age of mineralization must be as old as or younger than these tectonic elements. These are: (1) the Bou Jaber deposit is located at the edge of a salt diapir; (2) the diapir is located on the regional Hercynian Tajerouine fault reactivated during the Alpine orogeny; (3) the ores are located along E–W- to NE–SW-trending fault zones including the faulted Late Aptian/Late Albian unconformity, and ore-rich zones are concentrated at the intersection of the SW–NE with NW–SE faults. These tectonic elements were derived from the Eocene to Miocene tectonic events of the

Alpine orogeny. Thus the timing of the ore emplacement at Bou Jaber is most likely Eocene–Miocene time. Furthermore, this time of ore deposition coincides well with the maximum stratigraphic burial and subsequent hydrocarbon generation and migration into the Late Aptian reservoir trap adjacent to the salt diapir.

Sampling and analytical methods

About 100 samples of ankerite, sphalerite, galena, barite, and calcite, and Late Aptian carbonate-hosting rocks were collected from underground, open pit exposures and drill cores. Most samples were collected at the −63, −69 and −95 m levels of the mine and are representative of the A, B, and C ore bodies of the *Gîte de l'Est* (Fig. 4d). Within a given ore body, minerals were collected from different zones (e.g., sulfide rich, mixed barite/sulfide, and barite rich). Gypsum was obtained from Triassic evaporites outcropping on the north side of Jebel Bou Jaber and from other Triassic evaporite diapirs of the region. Mineral separates for C, O, S, Sr, Pb isotope analysis were prepared by handpicking or by use of a dental drill. Ore textures, mineralogy, and petrographic relationships were determined on hand samples on thin and polished sections using transmitted and reflected light microscopy. In the following analytical methods, mention of instrumentation trade names or commercial products does not constitute an endorsement of that particular equipment.

Fluid inclusion studies were carried out on a variety of minerals from the main stage of mineralization: sphalerite, barite, fluorite, and calcite. Samples were prepared as standard 200- to 400-μm-thick doubly polished wafers. The measurements were carried out at the Earth Sciences Department, Faculty of Sciences of the University of Tunis El Manar, using a Linkam THM600 freezing-heating stage. The system was calibrated using pure CO_2 fluid inclusions (−56.6 °C), the freezing point of H_2O (0 °C), and melting points of Merck standards. The precision was ±0.5 °C. Fluid salinities were calculated as weight percent NaCl equivalent (wt% NaCl eq.) using the equation of Bodnar (1993). Standard procedures were carried out, with initial petrography to determine inclusion types and paragenesis in order to select material for subsequent microthermometric measurements. The 200- to 400-μm-thick doubly polished wafers were also examined with an epi-fluorescent microscope to observe the fluorescence of hydrocarbon-bearing inclusions.

Fluid inclusions hosted in fluorite and barite samples were analyzed individually by laser ablation inductively coupled mass spectrometry (LA-ICP-MS). Inclusions were chosen that were clearly primary, occurring in growth zones, but in addition, fluid inclusion assemblages (FIAs) that were pseudosecondary and in some cases secondary in origin, were analyzed to determine the full range of possible fluid compositions in the ore deposit. Individual inclusions, or groups of small related inclusions, were analyzed by LA-ICP-MS using an Agilent 7500c mass spectrometer, combined with a Geolas ablation system. This system uses a Compex 103 ArF excimer laser with a wavelength of 193 nm and an energy density between 10 and 15 J cm^{-2} at the sample surface. The operating frequency of the laser was typically 5 Hz with spot sizes of 25 and 50 μm, the main criteria being that the size was greater than that of the inclusions. Several small inclusions could be ablated together to provide sufficient mass for analysis if inclusions were very small. The ablated material was transported from the ablation cell to an Agilent 7500c ICP-MS using 99.9999 % He flowing at 2 ml min^{-1} into a cyclone mixer where it was combined with the Ar carrier gas flowing at 1.02 ml min^{-1}. The mixer prolongs the signal from the ablated inclusions and improves precision by increasing the number of cycles through the selected elements and therefore the number of determinations of their ratio relative to Na. The instrument was operated in reaction cell mode using 2.5 ml min^{-1} 99.9999 % H_2 to remove interferences from ^{40}Ar on ^{40}Ca and from ^{56}ArO on ^{56}Fe. Element/Na intensity ratios were converted to weight ratios using the NIST glass standard SRM-610. For K/Na the soda lime standard SRM-1412 was used in addition to SRM-610 as it has a K/Na ratio of 1 which was closer to the analyzed ratios of K/Na in barite while the K/Na ratios in fluorite are closer to the value of SRM-610. Instrumental drift was checked using SRM-610, which was insignificant over each day's analysis. Integration of the standard and sample signals used the SILLS software package (Guillong et al. 2008). Full details of the analytical protocols and calibration of the instrument are presented in Allan et al. (2005). The moderate to high salinities of the inclusions and their size enables the signal from the ablation of fluid inclusions to be easily distinguished from any matrix signal. The ablation of the host fluorite or barite precedes opening of the inclusions and continues after the inclusion signal has ceased. Therefore, any signal from the sample matrix is easily observed and can be removed by the SILLS software. The distinction between inclusion and matrix is based on the sharp rise and then decrease in the inclusion signal over a period of c. 10–15 s, whereas the matrix signal is more constant over the entire ablation period. In addition, areas of fluorite and barite that were free of inclusions were ablated for a total of 200 pulses to determine if they contained any significant concentrations of the elements to be determined in the inclusions. In fluorite-hosted samples there was no contamination from the matrix except for Ca and Sr in one sample. In barite there was considerable contamination from the mineral matrix for elements such as Fe, Zn, Sr, in addition to Ca and Ba from the fluid inclusion host mineral. This signal from the contamination could not be resolved from that of the fluid inclusions because it was too erratic.

Stable isotope analyses were obtained at the stable isotope laboratory of the US Geological Survey (USGS) Crustal

Geophysics and Geochemistry Science Center in Denver following the procedures of McCrea (1950) for carbonates and Giesemann et al. (1994) for sulfur minerals. Isotopic compositions are reported in δ-notation relative to VPDB for carbon, VSMOW for oxygen, and VCDT for sulfur. Precision of the analyses is better than ±0.1 ‰ (1σ) for carbonates, ±0.2 ‰ for sulfur, and ±0.5 ‰ for oxygen in sulfates.

Strontium isotope analyses were performed on nine barite separates and on one gypsum sample. Sample separates were finely milled, dried for 4 h, and then leached overnight in 6 N HCl at 100 °C. Dry residues were dissolved in 2.5 N HCl. After centrifugation, strontium was separated using standard cation-exchange procedures. Sr isotope ratios were measured on a thermal ionization mass spectrometer at the Centre Pétrographique et Géochimique (CRPG), Nancy, France. Strontium isotope deviation of analysis was usually ±0.00004.

Galena crystals for lead isotope analyses were selected by handpicking under a binocular microscope and then rinsed with doubly distilled water. Lead isotope analyses were performed using thermal ionization mass spectrometry (TIMS) at the Geochronology and Isotope Geochemistry Laboratory, University of North Carolina, Chapel Hill, following the procedure described by Skaggs et al. (2012) and Garnit et al. (2012).

Results

Ore textures and mineralogy

The ore mineralogy consists of three distinct mineral assemblages representing at least three hydrothermal events: (1) breccia-hosted sphalerite-galena ores with rare pyrite and some tetrahedrite micro-inclusions in galena; (2) cavity-filled barite-rich ores; (3) replacive and geodic fluorite (+ minor Pb-Zn sulfides). Post-ore calcite fills thin fractures. The hydrothermal alteration mineral assemblage is represented by ankerite and quartz. A generalized paragenetic sequence for the minerals at the Bou Jaber mine is given in Fig. 5.

Breccia-hosted sphalerite-galena ores (stage 1)

The sphalerite-galena ores are hosted in dissolution-collapse breccias and cavities crosscutting the unit 5 of the Late Aptian carbonates. Breccia elements are composed of light gray carbonate host rocks (2 cm to 2 m across) and are surrounded by black matrix (Fig. 6a–c). The latter is composed of kaolinitic mudstone, minor fine-grained cubic pyrite (20 to 150 μm in size), calcite relicts, organic matter debris and abundant fine-grained hydrothermal bipyramidal quartz (100–200 μm) (Fig. 6e–g). This black mudstone matrix is also observed in small veins and stylolites, and is the main host of sulfide (Fig. 6b–c). Sphalerite occurs as honey to light brown euhedral crystals 1 to 8 mm across, with a dark brown core (Fig. 6d–f). Galena is less abundant than sphalerite (Fig. 6b–c) and precipitated during and after sphalerite deposition as indicated by geometric relationships and overgrowths (Fig. 6g). Minor epigenetic galena crystals, 1 to 2 cm across occur as irregular disseminations that replaced the limestone wall rock. Both sphalerite and galena contain abundant inclusions of micrite grains (up to 200 μm), bipyramidal quartz (100–200 μm), organic matter (5–20 μm) and pyrite microcrystals (20–50 μm). These insoluble residues were inherited from the decalcification of the black matrix hosting the sulfide assemblage described below, as well as from the dissolution of Late Aptian carbonate host rocks. Bipyramidal quartz is the first hydrothermal alteration of the host rocks and pre-dates sulfide deposition. Only rare barite (barite-1) aggregates have been observed in the sulfide-rich ore zones or in laterally equivalent breccias, so it seems unlikely that the sulfides replaced barite in this deposit. The black mudstone-hosted sulfides may represent internal sediments, which is common in most carbonate-hosted deposits and districts where dissolution-collapse breccias are present, (Sass-Gustkiewics 1996; Leach and Sangster 1993; Matlock and Misra 1993; Bouabdellah et al. 1996).

Barite- and ankerite-rich ore (stage 2)

Barite-rich ores fill hydrothermal dissolution cavities up to several meters in diameter (Fig. 7a). The wall rocks of the cavities have been partly to completely replaced by coarse-grained ankerite (ank-1) that forms 5 to 20-cm-thick halos lining the barite-rich ore bodies. Ankerite-1 occurs as aggregates of well-formed rhombohedral crystals, 1 to 5 mm across (Fig. 7b). In numerous places, the barite-rich ores consist of alternations of white and black colored bands (Fig. 7c–d). The black bands are composed of black mudstone similar to that described above in the sulfide stage containing fine-grained quartz-barite-1-sphalerite-galena assemblage overprinted by aggregates of stage 2 ankerite (ankerite-2) which is commonly replaced by black fluorite-1 (see fluorite stage below). The white bands, 2 to 20 cm in thickness, are essentially composed of stacked or intergrown tabular barite crystals (barite-2), 0.5 to 3 cm thick and 2 to 20 cm long. In the central part of the barite-rich ore bodies, late-stage barite (barite-3) forms spectacular very large white to transparent barite crystals (50 cm to up to 1.5 m long and up to 10 to 30 cm thick) that occupy 80 to 90 % of the cavities (Fig. 7e).

Fluorite (+minor sulfides) (stage 3) and post-ore calcite

Massive dark to black fluorite (fluorite-1), with small amounts of sphalerite and galena, most commonly fills polygonal spaces between intergrown barite crystals. In detail, the fluorite-1 has partially to completely replaced the calcite and

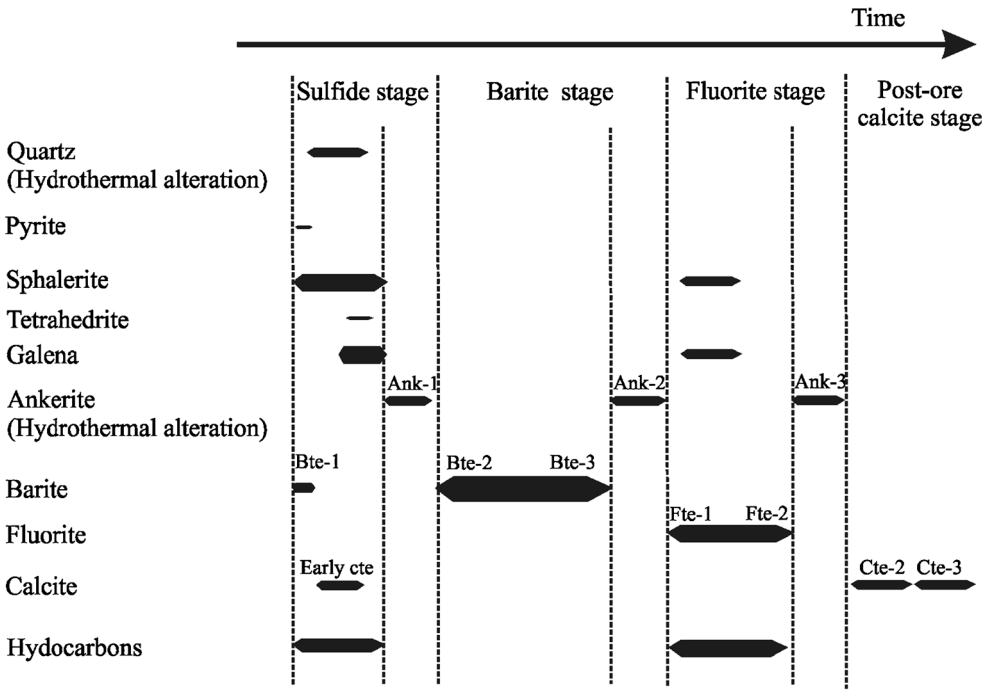

Fig. 5 Schematic paragenetic sequence of the ore-, and mineral alteration assemblages in the Bou Jaber (Gîte de l'Est) Pb-Zn-Ba-F deposit. Bars thicknesses reflect abundance of minerals. Hydrocarbons occur as oil seeps in the ore and as oil-bearing fluid inclusions in the sulfide and fluorite stages

ankerite that previously cemented sulfides and barite crystals (Fig. 7f). The black color of this fluorite is due to abundant solid inclusions (e.g., sphalerite, micrite, ankerite, black clay, and fine-grained hydrothermal bipyramidal quartz), and to abundant oil inclusions. Following the fluorite-1 stage, fluorite-2 (with minor Zn-Pb sulfides) forms geodic cubic crystals from few mm to 5 cm across, which are colorless or purple. This fluorite is commonly coated by rhombohedral crystals of ankerite up to 5 mm across (ank-3), and by late-stage calcite occurring as large scalenohedral crystals up to 5 cm across. Post-ore spar calcite occurs in thin open fractures (5 to 20 cm wide) crosscutting the previously described ores and the host rocks.

Fluid inclusion petrography and microthermometry

Few fluid inclusions are observed in sphalerite; however, barite, fluorite, and late-stage calcite contain numerous primary and secondary fluid inclusions suitable for fluid inclusion study. In these minerals, primary fluid inclusions were identified in the context of Roedder (1984) and Goldstein and Reynolds (1994). They are classified in three types (Fig. 8): (1) Liquid water + vapor ($L_w + V$); (2) Liquid petroleum + vapor ($L_P + V$); (3) Liquid water + liquid petroleum + vapor ($L_W + L_P + V$).

Aqueous fluid inclusions microthermometry

The microthermometric data derived from the primary fluid inclusions in sphalerite, barite, and fluorite from Bou Jaber *Gîte de l'Est* are given in Table 1. Sphalerite contains small (5 to 20 μm size) $L_w + V$ and $L_P + V$ fluid inclusions. Microthermometric analysis preformed on the $L_w + V$ inclusions yielded first melting temperature (T_{fm}) values in the range of −40 and −30 °C. The final ice melting temperatures (T_{mice}) vary from −18 to −13 °C with a mode at −16 °C. The homogenization temperatures (Th) range from 120 to 136 °C with a mode at 128 °C (±5 °C). Calculated salinities range from 17 to 20 wt% NaCl eq. with a mode at 19 wt% NaCl eq. (±1 %).

Transparent and geodic barite crystals (barite-2 and barite-3) contain numerous two-phase inclusions ($L_W + V$) (5 to 200 μm size) that form locally abundant clusters. Fluid inclusions indicating stretching or necking down (Roedder 1984; Ulrich and Bodnar 1988) were not measured. It is well known that barite is susceptible to stretching of the fluid inclusions by modest heating beyond their trapping temperature (Ulrich and Bodnar 1988). Therefore, only sets of primary fluid inclusions that had the same Th values are reported. Nevertheless, there is an unknown level of uncertainty regarding the Th data for barite, consequently the reported Th values, should be considered *maximum* temperatures for fluid trapping. In general the ($L_W + V$) inclusions present generally the same volumetric proportion of the liquid to vapor phases ($L = 90$ to 95 %; $V = 5$ to 10 %). The first melting temperature (T_{fm}) values range from about −45 to −19 °C (ave. −34 ± 7 °C, $n = 36$). The final ice melting temperatures (T_{mice}) range from −14 to −8 °C (ave. −10 ± 1 °C; $n = 31$). The homogenization temperatures (Th) range from 100 to 130 °C (ave. 114 ± 10 °C). Calculated salinities range from 11 to 15 wt% NaCl eq. (ave. 13 wt% NaCl eq. ± 1 %).

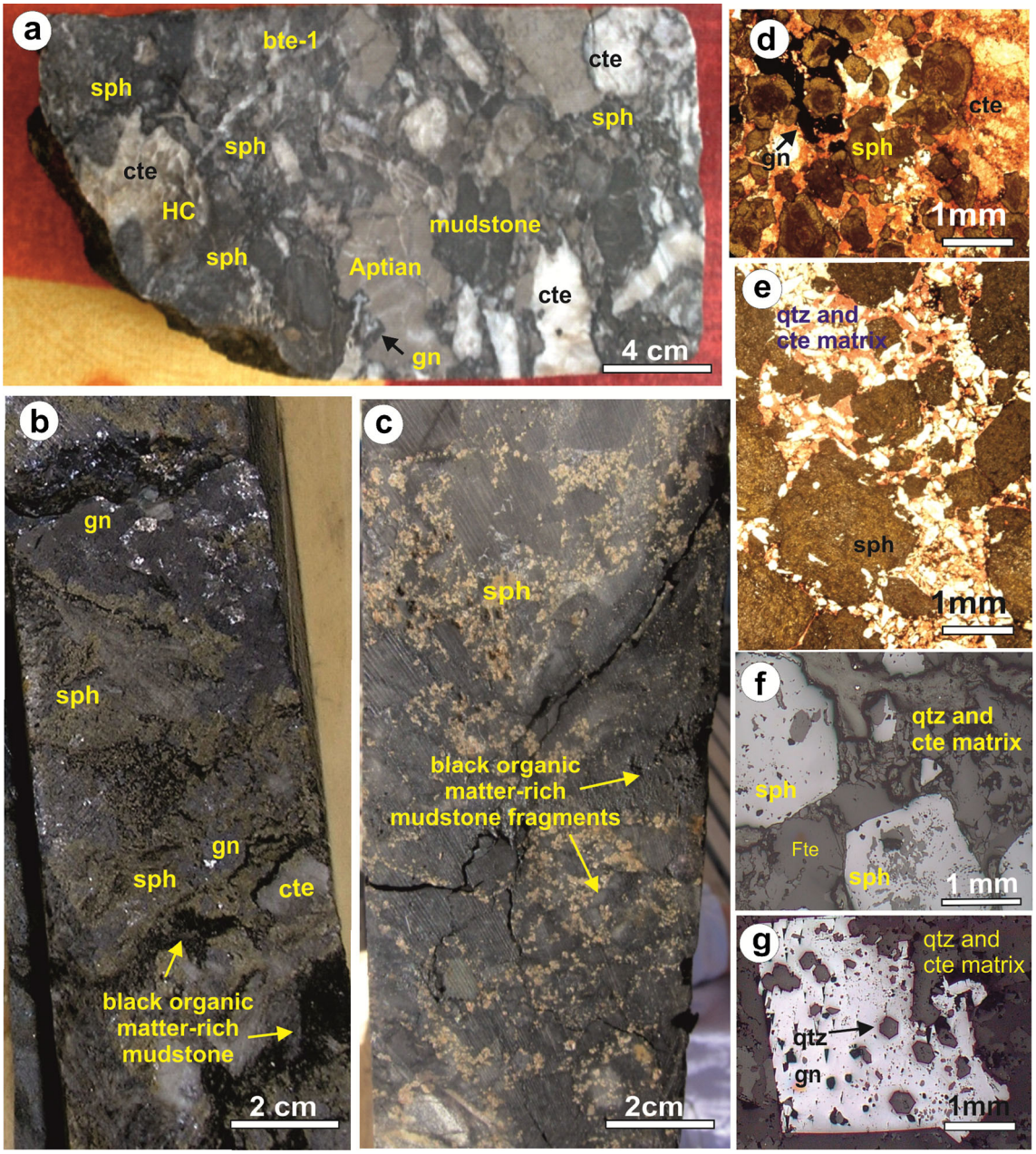

Fig. 6 Drill core samples of zinc lead-rich ore from dissolution cavities where sphalerite and galena occur by replacement of carbonaceous breccia matrix. **a** Dissolution breccia sphalerite-rich: Breccia fragments are grey Late Aptian limestone and black mudstone. The matrix is composed of fine-grained bipyramidal quartz, fine-grained honey sphalerite, galena, minor fine-grained barite-1 and calcite. Liquid hydrocarbon (HC) fills cavities in the calcite aggregations. **b** Core sample of high-grade massive sphalerite and galena. **c** Core sample of high-grade sphalerite (honey euhedral sphalerite crystals) aggregate in black mudstone breccia calcite-, quartz-, and organic matter-rich. **d** Detail from **c** showing sphalerite crystals cemented by calcite (red-S colored). **e** detail from **c** showing aggregations of euhedral sphalerite crystals in a quartz- and calcite-rich matrix; quartz is white and calcite is red-S colored. **f** Euhedral sphalerite in a matrix of calcite and quartz. Calcite is partly replaced by fluorite. **g** Euhedral galena containing bipyramidal quartz relicts of the replaced quartz-, calcite-rich sulfide matrix. **d** and **e** polished sections, transmitted light; **f** and **g** polished sections, reflected light

Fluorite-1 and fluorite-2 samples contain abundant two-phase inclusions ($L_W + V$) (5 to 200 μm size). The T_{fm} recorded temperatures range from −45 to −28 °C. The final ice melting temperature (T_{mi}) values vary from −20 to −12 °C with a mode of −17 °C. The homogenization temperatures range from 140 to 165 °C (mean = 152 ± 7 °C). Calculated salinities range from 16 to 23 wt% NaCl eq. with a mean of 20 ± 1.5 wt% NaCl eq.

Transparent late-stage calcite crystals (calcite-2), overlapping fluorite in druses and caves, contain small but numerous two-phase inclusions ($L_w + V$) of about 5

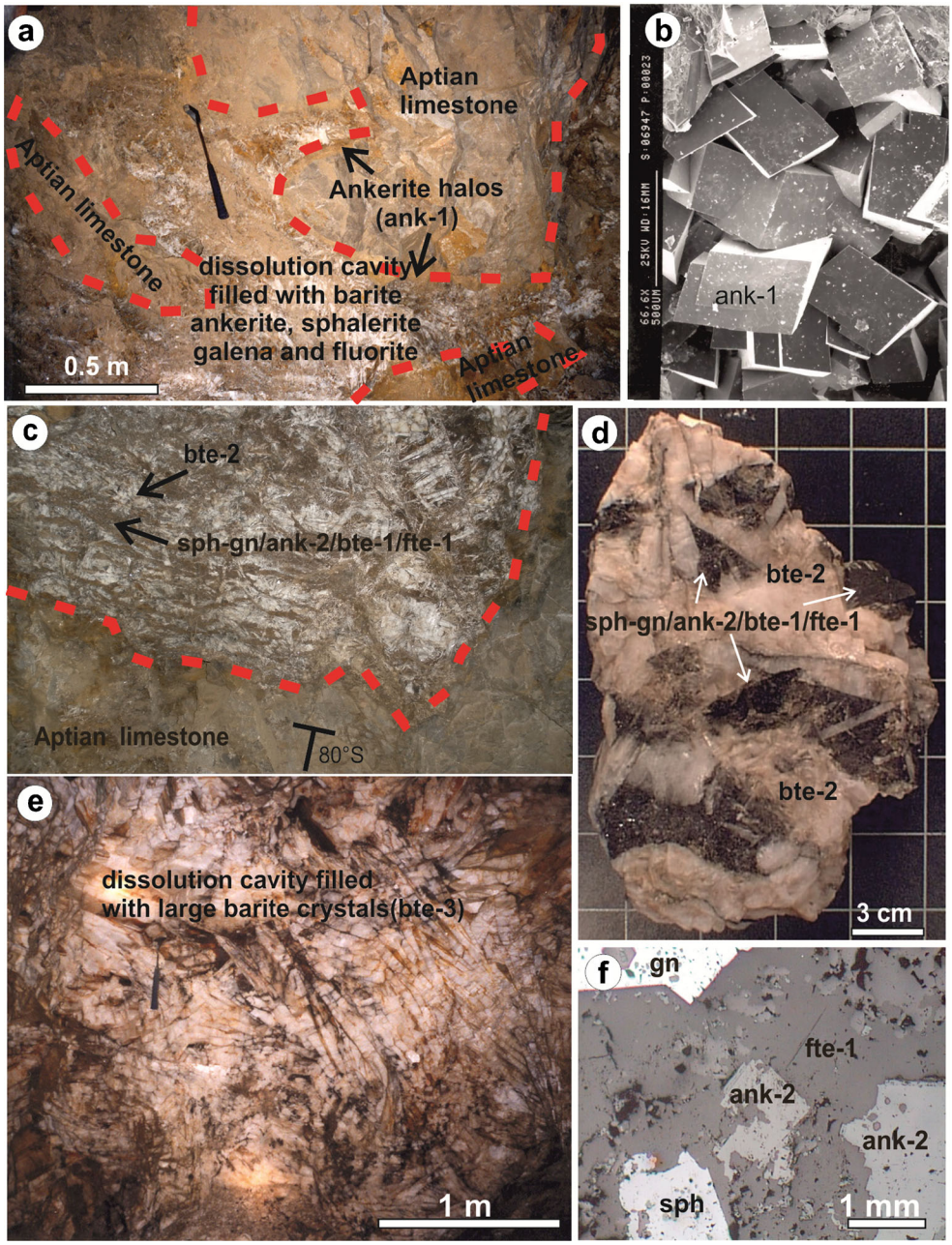

Fig. 7 Hydrothermal dissolution and ankeritization of the Late Aptian limestones (unit 5) followed by barite deposition in the Gîte de l'Est deposit. **a** Hydrothermal dissolution of the Late Aptian limestone developed large irregular cavities, meter- to plurimeteric-size. An ankerite halo (ank-1), 5- to 50 cm thick, lines the hydrothermal alteration of the host rock. The infilling material of cavities is composed of ankerite-2 and barite postdating minor sphalerite and galena. b SEM photograph of the euhedral coarse-grained ankerite crystals (ank-1) (sample from the ankerite halo). **c** Banded barite-rich ore in dissolution cavity, showing horizontal banding compared to the 70°deeping of the Late Aptian limestones strata. White bands are barite and dark bands are a complex assemblage of ankerite-2, sphalerite, galena and fluorite. **d** sample of banded barite-rich ore. The black matter is composed of ankerite and sulfide where most of the ankerite is replaced by fluorite (as shown on Fig. 8f). The white bands are composed of tabular centimeter-size crystals of barite developed often orthogonally to the dark bands. **e** barite zone formed by large barite crystals (central part of the hydrothermal dissolution cavities, underground working at level −95 m). Barite forms tabular crystals 5- to 20 cm thick and 50- to 100 cm length (scale is also shown by the hammer). **f** fluorite-1 replacing ankerite matrix of sphalerite and galena crystals, polished section, reflected light

to 50 μm size. The first melting temperature (T_{fm}) values range from −33 to −30 °C. The final ice melting temperatures (T_{mice}) were in the range of −18 to −15.5 °C with a mode of −17 °C. The homogenization temperatures (Th) range from 109 to 117 °C (ave. 114 ± 2 °C). Calculated salinities range from 19 to 21 wt% NaCl eq., with a mode of 20 wt% NaCl eq.

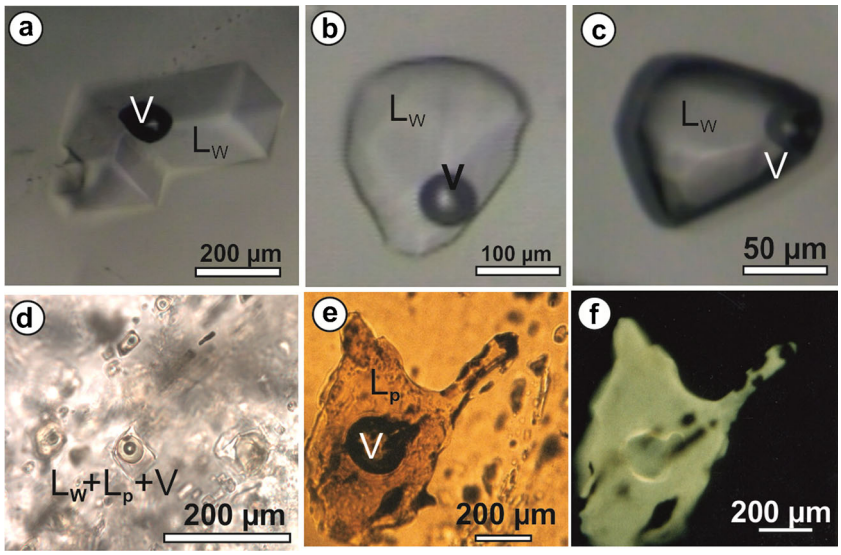

Fig. 8 **a** and **b** Primary $L_w + V$ fluid inclusions in fluorite. **c** Primary $L_w + V$ fluid inclusions in barite. **d** Primary $L_w + L_p + V$ fluid inclusion in fluorite. **e** Large primary $L_p + V$ fluid inclusion in fluorite. **f** Same as Fig e but under epifluorescence microscope. L_w = water; V = vapor; L_p = Petroleum

Petroleum fluid inclusions

Liquid hydrocarbon fluid inclusions are observed in sphalerite and are abundant in fluorite. The inclusions in sphalerite are less than 5 to 10 μm in size. Large inclusions (80 to 200 μm) are observed in the core or along growth zones of fluorite crystals. In black fluorite crystals, petroleum-bearing inclusions represent more than 30 % of the total inclusions. The black color of fluorite is due to petroleum inclusions.

Two types of primary fluid inclusions are observed: $L_p + V$ and $L_w + L_p + V$ fluid inclusions that are isolated or distributed along growth zones. These inclusions may coexist in the same mineral zones with aqueous inclusions ($L_w + V$). Secondary $L_w + V$ and $L_p + V$ fluid inclusions are located along fractures, cracks, and cleavage planes. In transmitted light, liquid hydrocarbon inclusions are usually brown- to yellow-colored. In epifluorescence observations, most of the hydrocarbon inclusions show fluorescence emissions in light yellow to light or deep blue colors.

Primary $L_p + V$ inclusions recorded homogenization temperatures that range from 97 to 140 °C, and are lower than the Th values of coexisting aqueous inclusions (100 to

Table 1 Summary of the microthermometric data derived from the study of primary fluid inclusions ($L_w + V$) in sphalerite, barite and fluorite from the Bou Jaber mine, levels −63, −69, and −95 m (Fig. 4d). Average values are reported in parentheses

Sample	Mineral	Nbr IF	Te °C	Tm ice °C	Salinity Wt% NaCl eq.	Th °C
2525C1	Sphal	38	−39 to −32	−16.8 to −14.8	18.5–19.1 (19.2)	112–133 (123)
2525C3	Sphal	34	−40 to–30	−18.7 to −13.4	17.3–21.5 (19.1)	115–136 (125)
6921D	Sphal	28	−40 to −37	−1.7 to −13.6	17.4–19.99 (18.1)	116–136 (128)
	Total		−40 to −30	−18.7 to −13.4	17.2–21.47 (19.1)	112–136 (125)
6925B1	Barite	20	−40 to −39	−11 to −7.8	11.5–15 (13.3)	101–110 (105)
9514BA	Barite	10	−43 to −40	−11.4 to −7.6	11–15 (13.6)	116–124 (120)
95 J1	Barite	16	−40 to −38	−10.4 to −8.8	12.6–14.4 (13.2)	110–114 (112)
9533B	Barite	25	−42 to −36	−10 to −8.8	12.6–13.9 (13.4)	100–131 (119)
63WA	Barite	18	−45 to −41	−13.6 to −11.6	15.6–17.4 (16.7)	115–118 (117)
	Total	89	−45 to −36	−13.6 to −7.6	11.2–17.4 (13.9)°	100–131 (114)
8511	Fluorite	34	−42 to −28	−18 to −14	21.5–18.1 (20.1)	140–165 (155)
B8512	Fluorite	60	−42 to −28	−13.8 to 19.4	22–17.6 (19.8)	144–163 (154)
9514AF	Fluorite	52	−32 to −28	−19.6 to −15.8	22.1–19.3 (20.6)	140–163 (150)
95514BF	Fluorite	60	−32 to −28	−20.5 to −15	22.6–18.6 (20.5)	144–162 (153)
9533BF	Fluorite	40	−45 to −40	−18.2 to −12.4	21.1–16.3 (17)	146–154 (145)
	Total	246	−45 to −28	−20.4 to −12.4	16.3 –22.6 (20)	140–165 (152)
63WB	calcite	25	−33.3 to −30	−18.2 to −15.5	20–0.9 (20.8)	113–126 (118)
63WC	calcite	22	−33.3 to −30	−18 to −17	21.1–19.0 (20)	109–117 (113)
	Total	45	−33 to −30	−18.2 to −15.5	19.0–21.1 (20.5)	109–126 (116)

165 °C). The differences in homogenization temperatures are about 20 °C which probably reflects differences in pressure corrections caused by the greater compressibility of oil than water (Roedder 1963).

Semi-quantitative compositions of hydrocarbon inclusions trapped in barite and fluorite crystals were determined by infrared microscopy and microfluorometry, as described in Guilhaumou et al. (1990). Both techniques show the presence of aliphatic and aromatic components in the oil, but microfluorometry shows that in barite the components are aliphatic dominant and in fluorite aromatic compounds dominate. The transition from aliphatic-rich oil inclusions to more aromatic components correlates with the timing and temperature of barite to fluorite deposition. The temperatures associated with the deposition of barite are low at around 100 to 130 °C, whereas in fluorite the temperatures are higher at around 140 to 165 °C. The loss of the aliphatic structures in the kerogen from the barite to fluorite event is consistent with a longer residence time for the source rocks at higher temperatures.

Homogenization temperature-salinity relationships

Salinities and homogenization temperatures from primary fluid inclusions ($L_w + V$) in sphalerite, barite, fluorite, and calcite are shown in Fig. 9. The data indicate that sphalerite, barite, fluorite, and late-stage calcite were probably deposited from fluids with homogenization temperatures in the range from 100 to 165 °C (ave. 130 °C ± 18 °C) and salinities in the range from 11 to 22 wt% NaCl eq. (ave. 17.5 ± 3 wt% NaCl eq.).

Based on the mineral paragenesis and the defined mineralization stages, the brine fluids are of four types: (1) the fluid that deposited sphalerite (A fluid) is characterized by high salinities (17 to 24 wt% NaCl eq.), and homogenization temperatures (112 to 136 °C); (2) the fluid responsible for barite deposition (B fluid) is characterized by lower salinities (11 to 17 wt% NaCl eq.), and lower temperatures (Th = 100 to 130 °C); (3) fluorite was deposited by fluids (C fluid) with salinities ranging from 19 to 21 wt% NaCl eq. (ave. 20 %), and relatively high homogenization temperatures of 140 to 165 °C; and (4) late-stage calcite was deposited by a fluid (D fluid) with Th ranging from 109 to 117 °C and calculated salinities from 19 to 21 wt% NaCl eq. (mode at 20 wt% NaCl eq.). The mean temperatures of the ore fluids decreased from sphalerite (125 °C) to barite (115 °C) and increased during fluorite deposition (152 °C); then decreased to ~110 °C during the late-stage calcite precipitation.

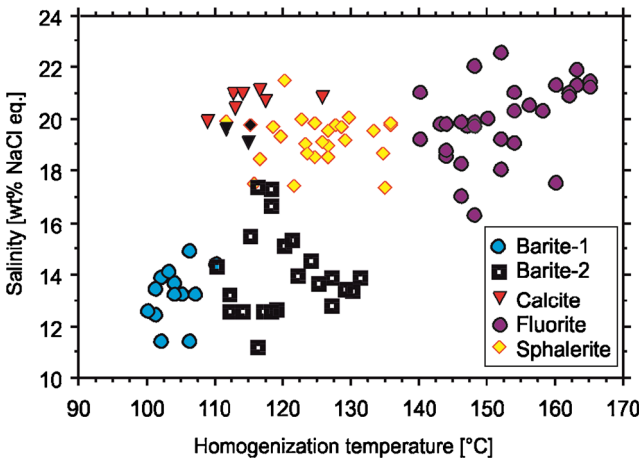

Fig. 9 Plot of Th versus salinity derived from microthermometric study of fluid inclusions in sphalerite, fluorite, barite and calcite

Composition of fluid inclusions using LA-ICP-MS

Approximately 200 fluid inclusions hosted in fluorite and barite were analyzed individually by LA-ICP-MS. A summary of the element/Na weight ratios for individual fluid inclusions and their reproducibility (based on more than 30 measurements for each sample) is presented in Table 2. The average weight ratios have also been converted to elemental concentrations (ppm) based on the average salinity of the inclusions in fluorite (18 equiv. wt% NaCl) and barite (13 equiv. wt% NaCl) determined by microthermometry (Banks et al. 2000). The accuracy of the calculation relies on the ability to measure all of the cation/Na ratios in the inclusion which is impossible for Ca and Ba because these are the cations in the host mineral. In fluorite it was possible to estimate the Ca/Na ratio from the ice and hydrohalite melting temperatures and using the NaCl-$CaCl_2$-H_2O phase diagram to calculate the Na/Ca ratio, which was found to be approximately 0.5. In barite, Ca is present as $CaCO_3$ and CaF_2 solid inclusions in the mineral matrix and contaminates the fluid analyses. It was also not possible to observe the ice-hydrohalite melting relationship in these inclusions; therefore, it was not possible to directly estimate the Ca/Na ratio of these inclusions. Based on similarities between other elements in fluorite- and barite-hosted inclusions, we assume the Ca/Na ratio to be similar to that in fluorite. In the barite, the ratios of Ba, Zn, and Sr to Na were also unreasonably high and were clearly from contamination in the host mineral.

The fluid inclusions in fluorite are dominated by Na > Ca > K > Mg, with the concentrations of Sr, Fe, and Zn each being equivalent to that of Mg. Concentrations of ore metals are 250 to 450 ppm Cu, 850 to 2100 ppm Zn, and 150 to 430 ppm Pb. The difference in the concentrations between the different fluorite-hosted fluids are, in the majority of cases, statistically significant and not due to the precision of the replicate analyses. The composition of the major cations in the barite-hosted inclusions is different than that in fluorite. The barite-hosted inclusions are dominated by K > Na > Ca > Mg, with Cu and Pb at significantly lower concentrations than in fluorite. Due largely to the different K/Na ratios, bivariate plots of pairs of individual inclusion analyses

Table 2 LA-ICP-MS analyses of individual fluid inclusions in fluorite and barite from Bou Jaber mine, levels −69 m and −95 m (Fig. 4d)

	BJ9533 Fluorite				BJ6921 Fluorite				BJ6925 Fluorite				BJ9533 Barite			
	Average wt/wt	StdDev	%RSD	ppm	Average wt/wt	StdDev	%RSD	ppm	Average wt/wt	StdDev	%RSD	ppm	Average wt/wt	StdDev	%RSD	ppm
Li	0.00595	0.0020	35.1	243	0.00415	0.0013	31.9	164	0.00685	0.0019	28.1	275	0.00433	0.0020	48.4	84
Na	1	0	0	40914	1	0	0	39527	1	0	0	40076	1	0	0	19334
Mg	0.01926	0.0143	74.5	788	0.05365	0.0259	48.4	2121	0.03236	0.0041	12.9	1297	0.03417	0.0169	49.5	661
K	0.09236	0.0740	80.2	3779	0.05780	0.0200	34.7	2285	0.13307	0.0842	63.3	5333	1.08053	0.3561	33.0	20891
Ca	*0.5*			*20457*	*0.5*			*19764*	*0.5*			*20038*	*0.5*			*9667*
Mn	0.00364	0.0018	50.0	149	0.00529	0.0034	64.4	209	<0.00595			<238	0.00714	0.0065	91.7	138
Fe	0.02681	0.0189	70.5	1097				0	0.04296	0.0325	75.8	1722	0.00974	0.0141	144.8	188
Cu	0.00624	0.0073	118.3	255	0.00935	0.0041	44.7	370	0.01115	0.0004	3.9	447	0.00745	0.0043	57.8	144
Zn	0.02107	0.0092	43.7	862	0.05745	0.0196	34.2	2271	0.02813	0.0325	115.8	1127				0
Sr	0.03196	0.0120	37.8	1308	0.05385	0.0195	36.3	2129				0				0
Ag	0.00005	0.0000	85.7	2	0.00024	0.0002	88.8	9	0.00067	0.0006	101.4	27	0.00037	0.0003	83.7	7
Ba	0.01409	0.0078	56.0	576	0.04720	0.0221	47.0	1866	0.00690	0.0038	56.2	276				0
Pb	0.01072	0.0085	79.8	439	0.00382	0.0021	55.9	151	0.00589	0.0060	103.3	236	0.00193	0.0008	41.4	37
U	0.00001	0.0000	95.5	0.3	0.00013	0.0001	141.8	5	0.00043	0.0003	72.9	17	0.00005	0.0000	26.1	1

Concentrations in fluorite are based on a salinity of 18 wt% NaCl eq., barite salinity of 13 wt% NaCl eq., Ca/Na wt ratio is based on hydrohalite-ice melting temperatures in fluorite and assumed to be the same for inclusions in barite (not possible to measure)

(Fig. 10a–l) show there are two distinct fluid compositions, whereas other ratios, such as Mg, Li, Sr, Cu, Pb, and Mn/Na are broadly similar. The elemental ratios of the three fluorite samples largely overlap indicating a common fluid. Differences in Mg/Na and K/Na between samples BJ9612 and the other samples are real but not significant enough to indicate these inclusions contain another distinct fluid.

Isotope geochemistry

Carbon and oxygen isotopes in carbonates

The isotopic results for barren Late Aptian limestones ($n=4$), mineralized limestone ($n=9$), ore ankerite ($n=8$), and post-ore calcite ($n=18$) are listed in Table 3 and shown on Fig. 11.

The limestone samples have $\delta^{13}C$ values ranging from −2 to 3.9 ‰ and $\delta^{18}O$ values ranging from 26.2 to 30.1 ‰, within the ranges typical of marine limestone of Cretaceous age (Veizer and Hoefs 1976; Land 1980). The values are comparable to values reported for Late Aptian limestones elsewhere in central Tunisia and eastern Algeria (M'Rabet 1987; Bouzenoune and Lécolle 1997).

Ankerite-1 ($n=3$) which precipitated after the sulfide stage and before barite, has $\delta^{13}C$ values of 2.7 to 3.6 ‰ and $\delta^{18}O$ values of 26.8 to 26.9 ‰. Ankerite-2 ($n=3$), which precipitated after barite, has $\delta^{13}C$ values of 2.4 to 3.6 ‰ and $\delta^{18}O$ values of 26 to 27 ‰. Ankerite-3 ($n=3$), which precipitated in geodes after fluorite, has $\delta^{13}C$ values of −0.5 to 1.5 ‰ and $\delta^{18}O$ values of 19.6 to 22.9 ‰.

Five samples of early calcite (calcite-1), which precipitated in geodes after fluorite-2 and ank-3, have $\delta^{13}C$ values of 1.3 to 3.8 ‰ and $\delta^{18}O$ values of 18.8 to +23.1 ‰. Late calcite (calcite-2) ($n=11$) has $\delta^{13}C$ values of 2.6 to 6.2 ‰ and $\delta^{18}O$ values of 24.8 to 27.4 ‰.

The $\delta^{13}C$ values of host limestone and hydrothermal ankerite are quite uniform: 2.0 ± 1.9 ‰ for the limestone, 3.1 ± 0.5 ‰ for pre-barite ankerite, 2.6 ± 0.3 ‰ for post-barite ankerite, and 0.5 ± 1 ‰ for post-fluorite ankerite. The isotopic similarity indicates that carbon in all three ankerite generations was derived from the local Late Aptian carbonates, and that carbon isotopic equilibrium was established between hydrothermal fluids and the host limestone during the main stages of ankerite and sulfide precipitation. Late-stage calcite shows higher $\delta^{13}C$ values (3.6 ± 1 ‰).

The oxygen isotopic composition of the limestone host rock is restricted to a narrower range (26.2–30.1 ‰) than the hydrothermal ankerite and calcite generations (19.6–27.4 ‰). The limestone represents the isotopically heaviest carbonates. The $\delta^{18}O$ values display a general downward trend in the following sequence: limestone (26.2–30.1 ‰) → pre-barite ankerite (26.8–26.9 ‰) ≈ post-barite ankerite (26.8–26.9 ‰) → post-fluorite ankerite (19.6–22.9 ‰) ≈ post-fluorite calcite (18.8–23.1 ‰). This trend resembles similar trends that have been observed at other MVT deposits (e.g., Frank and Lohmann 1986; Nesbitt and Muehlenbachs 1994; Spangenberg et al. 1996) in which isotopically lighter O is seen in paragenetically late carbonates compared to the unaltered host carbonates. The

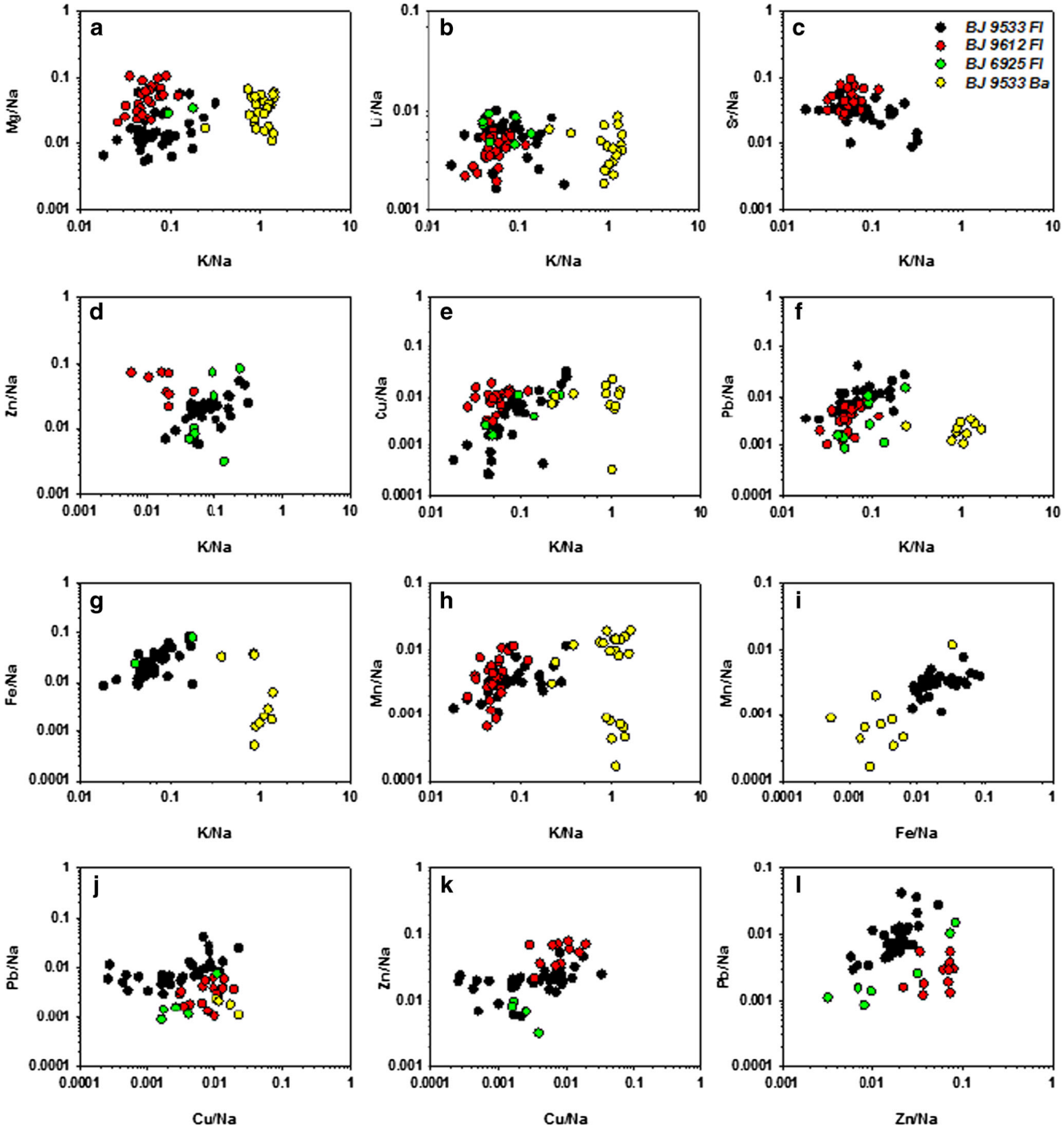

Fig. 10 Bivariate cation/Na weight ratios as determined by LA-ICP-MS of fluid inclusions. Inclusions hosted in barite are distinctly different than those in fluorite indicating two fluids involved in mineralization. Analyses from individual samples are tightly clustered and largely overlap for different fluorite samples

carbonates exhibit a positive covariation in a $\delta^{13}C$ vs $\delta^{18}O$ plot.

Sulfur isotope characteristics in sulfides and sulfates

Sulfur isotopic compositions were determined on 18 sphalerite, 43 galena, 3 pyrite, 45 barite, and 22 gypsum samples (Table 4, Fig. 12). The pyrite samples have $\delta^{34}S$ values of about 16‰, and sphalerite ranges from 8.4 to 9.8‰. There are no significant differences in sphalerite compositions among different sampled ore bodies, or within ore zones in a single ore body, or even among sulfide stages. Galena samples associated with the analyzed sphalerite range from 1.1 to 9.6‰. Most of the galena $\delta^{34}S$ values occupy a narrow

Table 3 Carbon and oxygen isotopes compositions of Aptian limestone host rock, hydrothermal ankerite and calcite from Bou Jaber mine

Samples	Description	$\delta^{13}C$ ‰ (VPDP)	$\delta^{18}O$ ‰ (VSMOW)
6928	Aptian limestone	−1.9	30.1
B6930A	Aptian limestone	2.7	29.6
B6929	Aptian limestone	2.6	29.9
9523U5	Aptian limestone	3.3	28.3
9549BC1	Aptian limestone	−2	27.9
69U5C1	Aptian limestone	2.7	26.9
69U5C2	Aptian limestone	3.9	26.2
6929U5	Aptian limestone	2.6	28
BJU5	Aptian limestone	1.8	27.3
BJU5 cte2	Aptian limestone	1.6	26.7
6939U5	Aptian limestone	2.9	26.7
9518U5	Aptian limestone	3	27.3
6937A	Aptian limestone	3.5	27
B9514	Ankerite 1	2.7	26.8
9534B1	Ankerite 1	3.6	26.9
9534B2	Ankerite 1	3.1	26.9
9534A2	Ankerite 2	3	27
B9517A	Ankerite 2	2.5	26.3
B9517B	Ankerite 2	2.4	25.9
9575A	Ankerite 3	−0.4	19.6
9575B	Ankerite 3	0.3	21.2
B63W	Ankerite 3	1.5	22.9
BJ901 cte	Calcite 1	1.3	18.8
B8511G	Calcite 1	1.3	21.7
C18015*	Calcite 1	3.1	22.9
C18128*	Calcite 1	3.3	21.3
B92H	Calcite 1	3.8	23.1
B9530B	Calcite 2	3.1	24.8
B6911B	Calcite 2	3.1	26
9502	Calcite 2	2.6	25.6
9505	Calcite 2	3.7	25.9
6904A	Calcite 2	2.9	25.5
C18028*	Calcite 2	3.6	26.9
C1830*	Calcite 2	3.8	27.1
C18020*	Calcite 2	3.8	27.4
BJ2295	Calcite 2	6.2	26.4
9549B	Calcite 2	3.5	25.6
B6937B	Calcite 2	3.3	27.3

[a] Analyses by Salmi-Laouar 2004; and from Salmi-Laouar et al. 2007

interval between 5 and 6 ‰. There is no significant difference between galena that replaced the breccia matrix in dissolution cavity-type ores (1.1–8.2 ‰; ave. 5.7 ‰), and epigenetic galena porphyroblasts in the host rocks or galena associated with the fluorite stage event (3.2–9.6 ‰; ave. 6.6 ‰).

The $\delta^{34}S$ values of Triassic gypsum range from 13.4 to 17.0 ‰ (ave. 15 ‰, $n=12$) similar to the previously reported

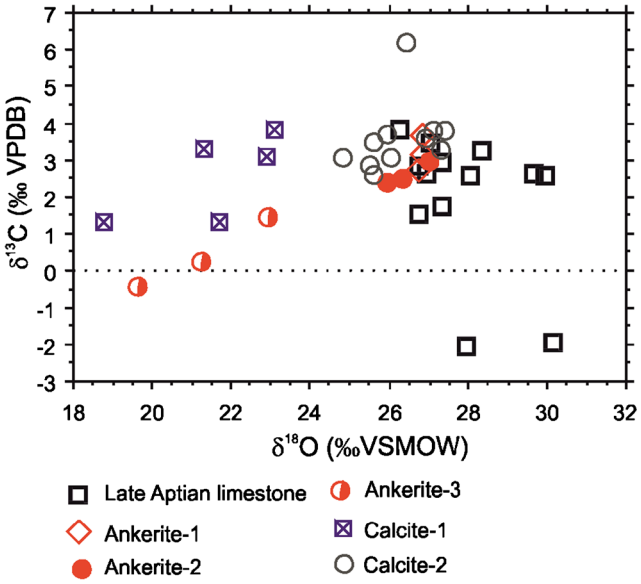

Fig. 11 Diagram $\delta^{13}C$ (‰VPDP) vs $\delta^{18}O$ (‰VSMOW) showing values for ankerite and calcite compared to the Late Aptian limestone host rock (Bou Jaber deposit)

compositions for Triassic gypsum of the TSDP (Sheppard et al. 1996; Salmi-Laouar et al. 2007). These values match the $\delta^{34}S$ values of Triassic seawater (13–16 ‰) (Claypool et al. 1980; Kampschulte and Strauss 2004).

The $\delta^{34}S$ values of barite range from 18.4 to 24.5 ‰ (ave. 22 ‰, $n=45$) (Table 4, Fig. 12a–b). Despite their wide spatial distribution, either within a single ore body or throughout the three ore bodies, the barite samples show a relatively narrow range of $\delta^{34}S$ values.

Oxygen isotope characteristics in sulfate minerals

The $\delta^{18}O$ values for Triassic gypsum range from 13 to 16 ‰, in good agreement with the $\delta^{18}O$ value of marine sulfate in Triassic time (Claypool et al. 1980). The $\delta^{18}O$ values of barite vary between 19.6 and 23.5 ‰ (ave. 22 ‰, $n=13$). The higher values imply that barite did not form simply by dissolution and re-precipitation of Triassic evaporite minerals. In fact, the barite $\delta^{18}O$ values are higher than the value of marine sulfate of any age (Claypool et al. 1980). Thus, rather than reflecting the source of the sulfate, the values reflect either isotopic exchange, possibly involving oxygen exchange with H_2O driven by hydrothermal heating, or a reservoir effect associated with partial reduction of a fixed sulfate pool.

Radiogenic isotopes

$^{87}Sr/^{86}Sr$ ratio in barite and gypsum

In order to constrain the origin of high-barium fluids and to monitor possible changes in fluid composition during barite deposition, nine samples of barite from the main barite stage

Table 4 Sulfur and oxygen isotopes compositions of sphalerite, galena, pyrite, and barite collected from different ore zones at levels −63, −69, and −95 m of the Bou Jaber mine (Fig. 4d); epigenetic galena and pyrite disseminated in Aptian limestone; and sulfur and oxygen isotopes compositions of Triassic gypsum collected from different salt diapirs of the area

Ore zones	Level (meter)	Samples	Mineral	δ^{34} ‰ (VCDT)	δ^{18}O ‰ (VSMOW)	Δ Sph-Gn ‰	T°C
Sulfide-rich zone	−63	1/P4Ba	Barite	21.5	21.3		
Sulfide-rich zone	−63	2/89NGn	Gn	5.8		3.6	176
Sulfide-rich zone	−63	3/89NGn1	Gn	6.0		3.5	180
Sulfide-rich zone	−63	4/89NSP1	Sph	9.4			
Sulfide-rich zone	−63	5/89NSP1	Sph	9.5		3.7	168
Sulfide-rich zone	−63	6/89NBa1	Barite	22.6	21.7		
Sulfide-rich zone	−63	7/89V2Sp	Sph	9.5		4	152
Sulfide-rich zone	−63	8/89V1Sp	Sph	9.5			
Sulfide-rich zone	−63	9/89V1Gn	Gn	5.5			
Sulfide-rich zone	−63	10/89V1Ba	Barite	23.4			
Sulfide-rich zone	−63	11/89V2Sp	Sph	9.2			
Sulfide/barite zone	−63	12/90K1Gn	Gn	3.6			
Sulfide/barite zone	−63	13/90K2Gn	Gn	5.2			
Sulfide/barite zone	−63	14/90K3Gn	Gn	5.2			
Sulfide/barite zone	−63	15/90K1Ba	Barite	20.2			
Sulfide/barite zone	−63	16/90K2Ba	Barite	22.3			
Sulfide/barite zone	−63	17/90K3Ba	Barite	21.1	22.2		
Sulfide/barite zone	−63	18/90K4Ba	Barite	21.6			
Barite zone	−63	19/6316Gn	Gn	6.37			
Barite zone	−63	20/63W4Ba	Barite	22.7	21.3		
Barite zone	−63	21/90CGn	Gn	5.8			
Sulfide-rich zone	−69	22/90HGSp	Sph	9.2		3.2	200
Sulfide-rich zone	−69	23/90HGn	Gn	6.0			
Sulfide-rich zone	−69	24/41AGn1	Gn	7.1			
Sulfide-rich zone	−69	25/11AGn2	Gn	8.1			
Sulfide-rich zone	−69	26/8511Gn1	Gn	1.1			
Sulfide-rich zone	−69	27/8511Gn2	Gn	1.2			
Sulfide-rich zone	−69	28/8511Sp1	Sph	8.4			
Sulfide-rich zone	−69	29/8511Ba1	Barite	21.5	21.8		
Sulfide-rich zone	−69	30/15Ba	Barite	21.9			
Sulfide-rich zone	−69	31/16BGn	Gn	6.7			
Sulfide-rich zone	−69	32/69BGn1	Gn	7.1			
Sulfide-rich zone	−69	33/69BBa	Barite	23.2	23.3		
Sulfide-rich zone	−69	34/20Sp1	Sph	9.3		4.48	129
Sulfide-rich zone	−69	35/20Gn1	Gn	4.9			
Sulfide-rich zone	−69	36/20Sp2	Sph	8.6		3.77	165
Sulfide-rich zone	−69	37/20Gn2	Gn	4.8			
Sulfide-rich zone	−69	38/20Ba1	Barite	21.6			
Sulfide-rich zone	−69	39/20Ba2	Barite	22.3			
Sulfide-rich zone	−69	40/21DSp1	Sph	9.7			
Sulfide-rich zone	−69	41/21DGn	Gn	8.2			
Sulfide-rich zone	−69	42/21DBa11	Barite	22.8			
Sulfide-rich zone	−69	43/21DBa12	Barite	23.0			
Sulfide-rich zone	−69	44/25C3Gn	Gn	5.8			
Sulfide-rich zone	−69	45/25DGn1	Gn	4.7		4.7	119
Sulfide-rich zone	−69	46/25DSp2	Sph	9.5			
Sulfide-rich zone	−69	47/25DGn2l	Gn	5.6			

Table 4 (continued)

Ore zones	Level (meter)	Samples	Mineral	δ^{34} ‰ (VCDT)	δ^{18}O ‰ (VSMOW)	Δ Sph-Gn ‰	T°C
Sulfide-rich zone	−69	48/25DGn3	Gn	7.5			
Sulfide-rich zone	−69	49/25Sp1	Sph	9.4		3.5	181
Sulfide-rich zone	−69	50/25Sp2	Sph	9.3		3.4	187
Sulfide-rich zone	−69	51/25Sp3	Sph	9.9		4.0	154
Sulfide-rich zone	−69	52/25Gn1	Gn	5.9		3.5	181
Sulfide-rich zone	−69	53/25Gn2	Gn	5.9			
Sulfide-rich zone	−69	54/27Sp	Sph	9.4		3.8	164
Sulfide-rich zone	−69	55/27Gn	Gn	5.6			
Sulfide-rich zone	−69	56/48Ba1	Barite	22.0			
Sulfide-rich zone	−69	57/48Gn1	Gn	5.1			
Sulfide-rich zone	−69	58/69DSp1	Sph	8.9			
Sulfide/barite zone	−69	60/21DBa1	Barite	22.9	20.7		
Sulfide/barite zone	−69	61/21DGn2	Barite	23.4	22.5		
Sulfide/barite zone	−69	62/21G1Gn	Gn	5.3			
Sulfide/barite zone	−69	63/21G1Ba	Barite	24.5			
Sulfide/barite zone	−69	64/23GGn1	Gn	6.5			
Sulfide/barite zone	−69	65/23GBa1	Barite	23.0			
Sulfide/barite zone	−69	66/25BGn	Gn	4.9			
Sulfide/barite zone	−69	67/25BBa	Barite	22.3			
Sulfide/barite zone	−69	68/36Gn	Gn	6.0			
Sulfide/barite zone	−69	69/36Ba2	Barite	22.2			
Barite zone	−69	70/31Ba	Barite	22.5			
Barite zone	−69	71/32Ba1	Barite	22.5			
Barite zone	−69	72/32Gn	Gn	5.5			
Barite zone	−69	73/32Ba2	Barite	20.8			
Barite zone	−69	74/BJDBa	Barite	22.4			
Barite zone	−69	75/50Gn1	Gn	5.9			
Barite zone	−69	76/69Ba	Barite	22.6			
Barite zone	−69	77/60Ba	Barite	23.7			
Sulfide-rich zone	−95	78/5AGn1	Gn	5.4			
Sulfide-rich zone	−95	79/5AGn2	Gn	5.6			
Sulfide-rich zone	−95	805ABa	Barite	22.3			
Sulfide-rich zone	−95	81/5Aba	Barite	18.7			
Sulfide-rich zone	−95	82/514gn	Gn	7.6			
Sulfide-rich zone	−95	83/514B2	Barite	22.8	23.1		
Sulfide-rich zone	−95	84/514AGn	Gn	5.6			
Sulfide-rich zone	−95	85/514ABa	Barite	21.2	21.8		
Sulfide-rich zone	−95	87/17AGn	Gn	7.9			
Sulfide-rich zone	−95	88/17Aba	Barite	21.3			
Sulfide-rich zone	−95	89/34BaG1	Barite	21.3			
Sulfide-rich zone	−95	90/34BaG2	Barite	18.5	21.4		
Sulfide/barite zone	−95	91/34BaG2	Barite	18.6			
Sulfide/barite zone	−95	92/33BaG2	Barite	22.8			
Sulfide/barite zone	−95	93/33BaG3	Barite	20.7			
Barite zone	−95	94/33BaG3	Barite	20.8			
Barite zone	−95	95/98K3Sp	Sph	9.7			
Barite zone	−95	96/98K3Gn	Gn	7.0			
Barite zone	−95	97/98K3Ba	Barite	20.8			
Barite zone	−95	98/98Ba	Barite	19.9			

Table 4 (continued)

Ore zones	Level (meter)	Samples	Mineral	δ^{34} ‰ (VCDT)	δ^{18}O ‰ (VSMOW)	Δ Sph-Gn ‰	T°C
Barite zone	−95	99/95K3Ba	Barite	23.4	23.4		
Barite zone	−95	100/C31Ba	Barite	21.3			
Barite zone	−95	101/60 int	Barite	23.0	21.8		
Barite zone	−95	102/60 ext	Barite	22.0	19.6		
Aptian limestone	Open pit	103*	Pyrite	15.6			
Aptian limestone	Open pit	104*	Pyrite	15.2			
Aptian limestone	Open pit	105*	Pyrite	16.2			
Aptian limestone	Open pit	106BJ1*	Gn	5.7			
Aptian limestone	Open pit	107CN*	Gn	7.2			
Aptian limestone	Open pit	108BJ2*	Gn	7.2			
Aptian limestone	Open pit	109 N6*	Gn	9.6			
Aptian limestone	Open pit	110 N2*	Gn	3.2			
Triassic sulfate	Ouenza	112 SA870*	Gypsum	16.0			
Triassic sulfate	Ouenza	113SA8729*	Gypsum	13.4			
Triassic sulfate	Ouenza	114SA8731*	Gypsum	14.3			
Triassic sulfate	Mesloula	115SA7982*	Gypsum	15.4			
Triassic sulfate	Mesloula	116SA8734*	Gypsum	15.2			
Triassic sulfate	Mesloula	117SA8738*	Gypsum	14.9			
Triassic sulfate	Mesloula	118SA8737*	Gypsum	15.3			
Triassic sulfate	Mesloula	119SA873*	Gypsum	14.6			
Triassic sulfate	Mesloula	120SA8733*	Gypsum	15.1			
Triassic sulfate	Mesloula	121SA8739*	Gypsum	15.5			
Triassic sulfate	Mesloula	122SA8740*	Gypsum	14.9			
Triassic sulfate	Bou Jaber	123S10*	Gypsum	15.4			
Triassic sulfate	Bou Jaber	124S40*	Gypsum	14.6			
Triassic sulfate	Bou Jaber	125S26*	Gypsum	15.3			
Triassic sulfate	Bou Jaber	126S26*	Gypsum	13.4			
Triassic sulfate	Bou Jaber	127S40*	Gypsum	15.3			
Triassic sulfate	Bou Jaber	128SA8726*	Gypsum	15.1			
Triassic sulfate	Hameimat	129SA8722*	Gypsum	13.4			
Triassic sulfate	Hameimat	130SA8735*	Gypsum	14.8			
Triassic sulfate	Fedj el Adoum	131 FH	Gypsum	16.0	15.5		
Triassic sulfate	Fedj el Adoum	132FH	Gypsum	17.1	12.9		
Triassic sulfate	Fedj el Adoum	133FH	Gypsum	16.8	16.1		

Calculated temperatures are obtained using the equation $\delta ZnS\text{-}\delta PbS = (0.73/T^2).10^6$ (Ohmoto and Rye1979)

[a] Analyzed by Salmi-Laouar 2004 and from Salmi-Laouar et al. 2007

were selected for $^{87}Sr/^{86}Sr$ analysis. In addition, one sample of anhydrite from the Triassic diapir was analyzed. Results of the $^{87}Sr/^{86}Sr$ analysis are listed in Table 5 and presented on Fig. 13. Regional $^{87}Sr/^{86}Sr$ ratios for Cretaceous sediments (Calvez et al. 1986) are also shown for comparison. A slight trend of ^{87}Sr-enrichment is observed from early to late generations of barite crystals. This trend indicates extensive exchange reactions between hydrothermal fluids and source rocks. A similar trend was observed in calcite generations in carbonate-hosted Pb-Zn deposits (Lange et al. 1983; Spangenberg et al. 1996).

Barite has Sr isotope compositions ranging from 0.709821 to 0.711408; these values are radiogenic compared to Triassic anhydrite with a $^{87}Sr/^{86}Sr$ ratio of 0.70800, which is close to the estimated ratio for seawater during Triassic times (0.7073 − 0.7080; Veizer and Compston 1974; Burke et al. 1982). The barite Sr isotope values are also more radiogenic than the Tunisian Cretaceous sediments (0.7074 to 0.7076; Orgeval 1994) that are close to the ratios of 0.7073 to 0.7075 for Cretaceous seawater (Koepenick et al. 1985). The radiogenic strontium of the Bou Jaber barite might reflect leaching of a feldspar-rich reservoir.

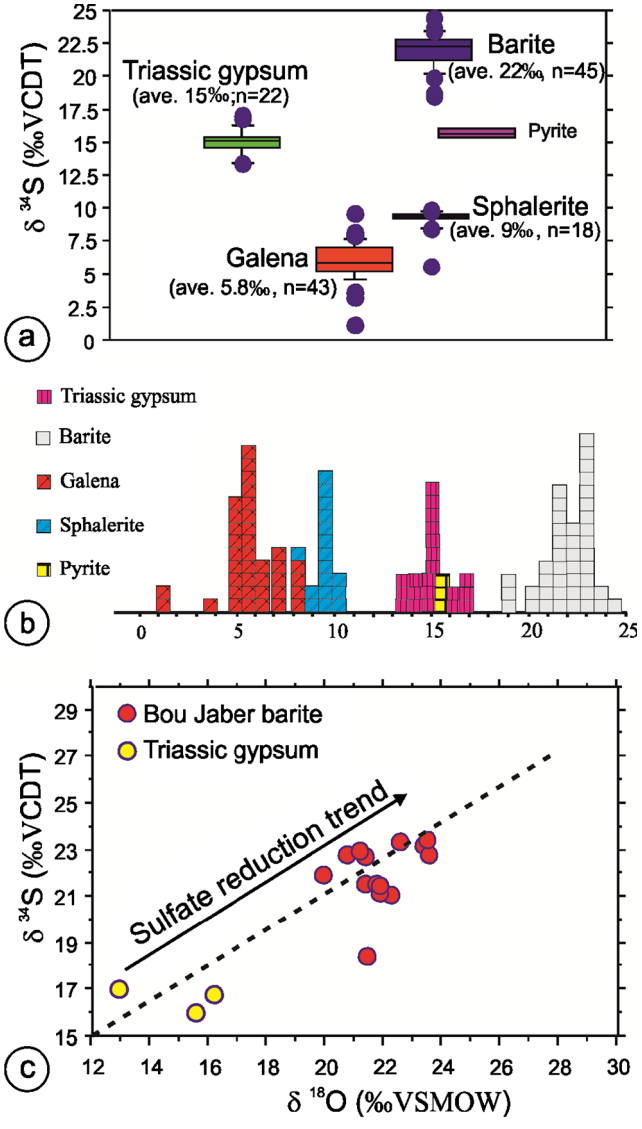

Fig. 12 **a** Box plot of $\delta^{34}S$ values for sphalerite, galena, pyrite and barite at Bou Jaber, and $\delta^{34}S$ values for regional Triassic gypsum. The sulfur isotope compositions shown are isotopically relatively homogeneous with a composition near 6 ‰ for galena, 9 ‰ for sphalerite, 22 ‰ for barite and 15 ‰ for Triassic gypsum. **b** Histogram distribution of the $\delta^{34}S$ values for sphalerite, galena, pyrite, barite and Triassic gypsum. **c** Plot of $\delta^{18}O$ vs $\delta^{34}S$ of Bou Jaber barites. The $\delta^{18}O$, $\delta^{34}S$ of Triassic anhydrite are also plotted for comparison with barites

Lead isotopes

Sixteen samples of galena were collected from the Bou Jaber ore deposit for lead isotope analysis. Results are presented in Table 6 and plotted in Fig. 14, and are compared to the sulfide lead composition of 24 Tunisian Pb-Zn deposits of the Tell thrust zone and the Atlas foreland (Bouhlel et al. 2013) and to the Pb isotope composition of a 15 Ma biotite microgranite sample from the Nefza region (Decrée 2008) and from Galite Archipelago on the Tunisian offshore (Juteau et al. 1986), about 120 and 150 km north of Bou Jaber, respectively (Fig. 1).

Table 5 Strontium isotope compositions of different barite generations from Bou Jaber mine (Gîte de l'Est, levels −69 m and −95 m) and of Triassic gypsum from the Bou Jaber Triassic salt diapir

Ore stage	Sample	Mineral	$^{87}Sr/^{86}Sr$	Std dev.
Early barite	69BJP4	Barite	0.708210	0.000031
Second generation barite	6960	Barite	0.710811	0.000026
Second generation barite	6932	Barite	0.710117	0.000029
Second generation barite	6921	Barite	0.710179	0.000032
Second generation barite	9531	Barite	0.710000	0.000033
Second generation barite	9514I	Barite	0.710134	0.000017
Late-stage barite	6960	Barite	0.710811	0.000026
Late stage barite	692G3	Barite	0.711408	0.000033
Late stage barite	6960G	Barite	0.711291	0.000031
Triassic sulfate	Triassic	Gypsum	0.708125	0.000044

The Bou Jaber galena samples have $^{206}Pb/^{204}Pb$, $^{207}Pb/^{204}Pb$, and $^{208}Pb/^{204}Pb$ values that range from 18.697–18.786 (ave. 18.729), 15.643–15.762 (ave. 15.679), and 38.7057–39.228 (ave. 38.842), respectively. The Pb isotope data form an arrow elliptic field in both $^{207}Pb/^{204}Pb$ versus $^{206}Pb/^{204}Pb$ and $^{208}Pb/^{204}Pb$ versus $^{206}Pb/^{204}Pb$ plots. The majority of the analyzed galena samples plot in a field below the upper crustal evolution curve (Fig. 14a) and above the orogen curve (Fig. 14b) indicating the dominance of continental crustal sources. Some of the galena samples plot clearly above the upper crustal curve (i.e., high μ), indicating a large component of a radiogenic source. Some others plot below the upper crustal curve, indicating a large component of non-radiogenic sources. The compositional field of Bou Jaber lies

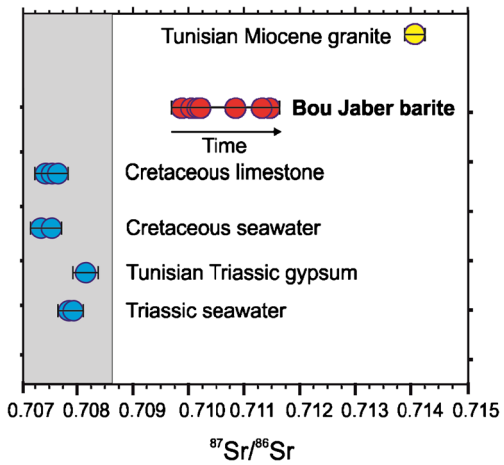

Fig. 13 Strontium isotope ratio diagram comparing Bou Jaber barite ores with Triassic evaporite, Triassic seawater (Veizer and Compston 1974; Burke et al. 1982), Cretaceous seawater (Koepenick et al. 1985) and with Tunisian Cretaceous sediments and with Tunisian Miocene granite ($^{87}Sr/^{86}Sr$ values for Cretaceous sediments are from Orgeval 1994 and for Miocene granite are from Juteau et al. 1986)

Table 6 Lead isotope composition of galena samples from Bou Jaber mine (Gîte de l'Est, levels −69 m and −95 m)

Samples	$^{206}Pb/^{204}Pb$	$^{207}Pb/^{204}Pb$	$^{208}Pb/^{204}Pb$
6911AGn1	18.737	15.643	38.767
6911AGn2	18.707	15.671	38.808
6921DGn	18.730	15.678	38.838
6925C3Gn	18.704	15.643	38.779
6925BGn1	18.699	15.649	38.751
6932Gn1	18.732	15.690	38.869
6936Gn1	18.707	15.670	38.806
6948Gn	18.719	15.668	38.797
6950Gn1	18.720	15.673	38.797
955ABGn1	18.783	15.762	39.100
698511G	18.733	15.664	38.816
955BGn1	18.786	15.757	39.085
9514AGn	18.755	15.664	38.821
9514BGn	18.699	15.646	38.736
9517Gn	18.729	15.686	38.838
9598 K3	18.752	15.663	38.805

within the lead isotope field defined by the major Tunisian Pb-Zn deposits in the TSDP representing the various ore deposit groupings within the Alpine thrust-belt and Atlas foreland (Bouhlel et al. 2013).

Given the homogeneous Pb-isotopic compositions of the Bou Jaber galena samples, it is reasonable to propose that the Bou Jaber ores were formed from fluids that passed through the same well-mixed source rock(s) over a relatively restricted period of time. Bou Jaber is located on the SW–NE-trending Tajerouine fault (Fig. 1), reflecting the main Paleozoic basement structural features that enabled diapirism and probably influenced fluid migration. It is possible that the lead may have been extracted from the basement or from siliciclastic feldspar-rich rocks in the basin, consistent with the $^{87}Sr/^{86}Sr$ ratios in barite.

The Pb-Zn ore isotopic lead field also overlaps that of the Miocene felsic rocks of La Galite Archipelago and the Nefza regions. These rocks, related to Miocene anatexis, were derived from a metaluminous basement (Belayouni et al. 2010). This feature may indicate that the ore lead and the felsic rocks were originally from similar source rocks, and/or probably extracted at the same period.

The Bou Jaber galena samples give $^{207}Pb/^{206}Pb$ model ages from the plumbotectonic model of Zartman and Doe (1981) between 400 and 300 Ma (Fig. 14a), older than the proposed Miocene age of the Atlassic metallogenic events (Sainfeld 1956; Rouvier et al. 1985; Bouhlel 2005). This retardation which was also observed for the Miocene felsic rocks (Decrée 2008) may be due to less radiogenic material with low uranium content such as the lower crust.

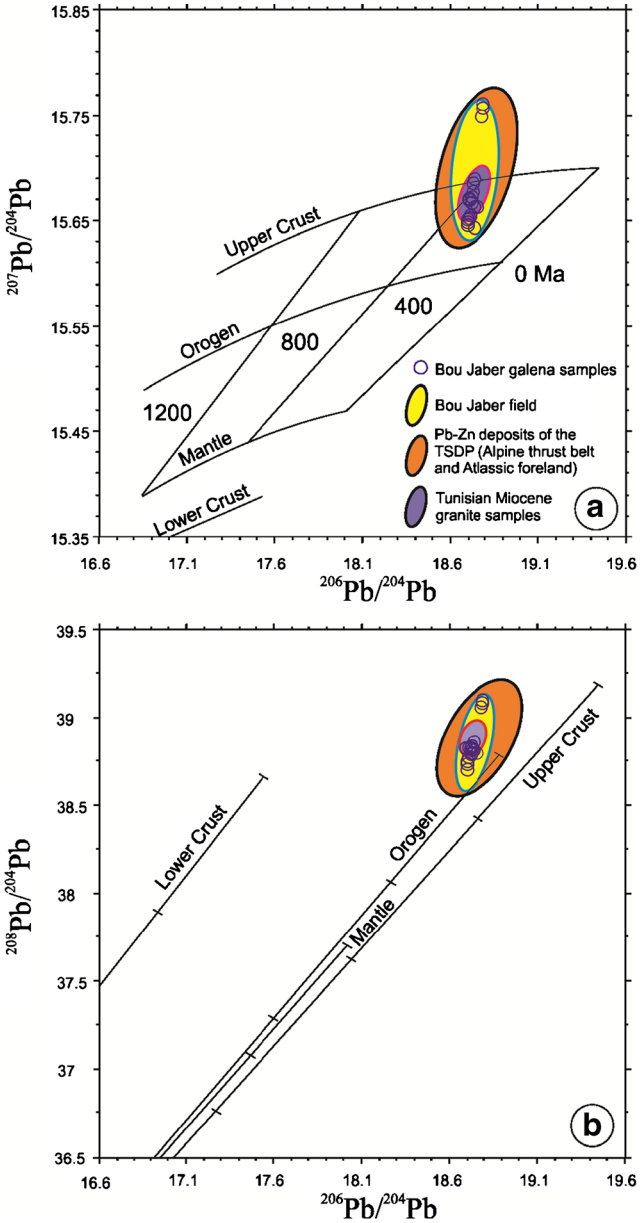

Fig. 14 Lead isotope ratios of galena samples from Bou Jaber Pb-Zn-Ba-F deposit reported in $^{207}Pb/^{204}Pb$ and $^{206}Pb/^{204}Pb$ diagram (14**a**) and in the $^{208}Pb/^{204}Pb$ and $^{206}Pb/^{204}Pb$ diagram (14**b**). Isotope composition are present-day values are not corrected to age. The upper crust, lower crust, orogen, mantle evolution curves are from Zartman and Doe 1981. Bou Jaber lead isotope compositions fill in the field determined from various Pb-Zn deposits groupings within the TSDP (Bouhlel et al. 2013). Bou Jaber lead isotope compositions are also compared to Pb ratios of Tunisian Miocene granite (values are from Juteau et al. 1986 and Decrée 2008)

Discussion

The recent identification of the giant Jinding lead-zinc deposit in China (200 Mt @ 6 % Zn + 1.3 % Pb) as diapir-related (Xue et al. 2007; Leach et al. 2013) has highlighted the economic importance of this deposit type. In the TSDP, Bou Grine (7.3 Mt @ 12 % Zn + Pb) is the most important representative of

this mineralization style. Other than the Bou Jaber deposit, fluorite is not present in the Pb-Zn rich ore-bearing diapirs either in Tunisia (e.g., Bou Grine, Fedj el Adoum) or in China (Jinding) nor is it reported from the Gulf Coast diapirs. Fluorite-rich diapirs, low in Zn-Pb mineralization are known both in Tunisia (e.g., the Zaghouan district; Bouhlel 1982; Bouhlel et al. 1988) and Morocco (e.g., Tirremi; Bouabdellah et al. 2013). However, a fluorite + barite (low Zn-Pb) ± calcite-dolomite-quartz mineral assemblage is more common in some vein deposits (e.g., US Central Tennessee, Leach and Sangster 1993); Zaghouan district, northeastern Tunisia, Bouhlel 1982, 1985; Bouhlel et al. 1988) and the Cevennes area, France; Macquar et al. 1990), particularly where basement-connected vein deposits cut the cover rock sequences.

Evidence for separate mineralizing events at Bou Jaber

The Bou Jaber ores display three mineral assemblages that are spatially and temporarily distinct: (1) Pb-Zn sulfides within dissolution-collapse breccias; (2) barite in dissolution cavities; (3) fluorite ores with minor sulfides that invade and crosscut the sulfide and barite ores. Figure 5 shows the paragenetic relations of these three events: the main stage of sphalerite and galena was followed by the barite event and finally by the fluorite event. The combined fluid inclusion temperature-salinity plot (Fig. 9) clearly shows three distinct groups based on salinities and temperatures for sphalerite, barite, and fluorite: a higher temperature-salinity field for fluorite, lower temperature-salinity field for barite, and an intermediate field for sphalerite. Although this distribution could possibly be interpreted as a cooling and dilution trend of a single fluid, the LA-ICP-MS analyses show the fluid inclusions in barite and fluorite have two different fluid compositions; no data are available on sphalerite. Inclusions in fluorite are metal rich (hundreds to thousands ppm Pb, Zn, Cu, Fe) but the inclusions in barite are metal deficient. Bivariant plots of pairs of individual inclusions analyses (Fig. 10a–l) show there are two distinct fluid compositions based largely on the different K/Na ratios while other ratios, such as Mg, Li, Sr, Cu, Pb, and Mn/Na are broadly similar.

Source of the ore fluids

The origin of high-salinity brines that form sediment-hosted Zn-Pb ores is generally attributed to evaporated seawater with or without involving some minor amount of dissolved halite. Although information on the composition of ore fluids in diapir-related ores are scarce, data for two diapir-related deposits, the Orduña-Murgía deposit in the Basque-Cantabrian basin, northern Spain (Grandia et al. 2003), and the Jbel Tirremi fluorite-barite deposit in Morocco (Bouabdellah et al. 2013), show the ore fluids were dominated by high-salinity brines representing a mixture of evaporated seawater and dissolved halite.

Regrettably, there are no data on the composition of the Zn-Pb ore fluids other than the fluid salinity from the fluid inclusions. Therefore, nothing can be concluded about the origin of the Zn-Pb fluids other than they plot in a temperature-salinity space (Fig. 9) that differs from the fluorite and barite fluids. Inclusions in fluorite from the Bou Jaber deposit have Cl/Br and Na/Br ratios of several thousand, consistent with dissolution of halite whereas the inclusions analyzed in barite have values lower than those of seawater, indicative of a Br-enriched brine derived from the evaporation of seawater plus a component of halite dissolution. The Bou Jaber fluorite ore fluids are Na-Ca dominated with low Mg concentrations indicating significant dolomitization of limestone by the fluids. The salinity of the barite fluids could be the result of evaporation of seawater prior to halite saturation or of dilution of a more saline fluid with meteoric water. Furthermore, the higher K/Na values of fluid inclusions from barite suggest the brines interacted with K-rich rocks in the basement or siliciclastic sediments in the basin. Oxygen isotope compositions of the ore fluid calculated from late-stage calcite indicate that the $\delta^{18}O$ of the fluid varied between ≈+3 and ≈+8 ‰. Such a fluid most likely originated from formation waters in isotopic equilibrium with the host rocks. The oxygen isotopic composition of the fluids that deposited the Bou Jaber Ba-F-Pb-Zn ores are similar to that of modern sedimentary basinal brines and MVT deposits (e.g., Mc Limans 1975, 1977) as well as to the nearby Fedj el Adoum deposit (Charef and Sheppard 1987).

Metal sources

The sources of metals in sediment-hosted ores are poorly understood. An extensive analysis of lead isotopes from sediment-hosted Zn-Pb ores (Leach et al. 2005) concluded that no single host rock type could explain the lead isotopic compositions of galena in the deposits. In many examples, the lead isotopic compositions of the ores suggest that the ore fluids may have interacted with the basement rock, the weathered regolith or basal sandstone or with detritus in the sedimentary cover rocks that contains material weathered from the basement rocks.

The lead isotope data from Bou Jaber indicate that the lead was derived from upper crustal rocks and it is reasonable to assume that these rocks were also the source of Zn, Fe and Ba. In Fig. 14, the isotopic data for Bou Jaber lie within the large field defined by Pb-Zn deposits of the Tell thrust-belt and the Atlas foreland. These regions have the same Precambrian–Paleozoic basement rocks, which suggest that the basement rocks or sediments derived from the basement likely contributed as metal sources in both regions. This suggestion is consistent with compilations of lead isotope compositions from global MVT ores (Leach et al. 2005) that suggest a

relationship between the isotopic composition of ores in a district and the composition of the corresponding basement rocks.

Barite from Bou Jaber has Sr isotope compositions that are radiogenic compared to Triassic anhydrite or the estimated ratio for seawater during the Triassic, and also more radiogenic than the marine Tunisian Cretaceous sediments. The most likely source for the more radiogenic strontium in the barite is feldspar-rich rocks.

The possible sources for fluorine are problematic. The common spatial association of world fluorite deposits with continental rift basins leads to the speculation that fluorine was possibly derived from deep-seated basement sources (i.e., mantle gases as in the Illinois fluorite district; Plumlee et al. 1994; Kendrick et al. 2002). This suggestion is consistent with the abundance of fluorite deposits adjacent to Mio-Pliocene graben structures in the Tunisian Atlas foreland (Fig. 1).

Sulfur source

Gypsum in the nearby Triassic salt diapirs is the most obvious sulfur source for the Bou Jaber ores. However, sulfate minerals or sulfate-bearing formation waters within overlying, younger strata would also be plausible sources inasmuch as ore formation did not occur until Miocene–Pliocene time.

The reduced sulfur in sphalerite and galena was most likely produced by thermochemical sulfate reduction (TSR). The evidence supporting this interpretation is two-fold. First, the minerals show relatively narrow isotopic ranges and relatively high $\delta^{34}S$ values compared with the ranges and values that commonly result from bacterial sulfate reduction (BSR) in marine sediments or marine rocks (Machel et al. 1995). Second, fluid inclusion microthermometry indicates that temperatures were sufficient to drive abiotic reactions between sulfate and organic matter ($80–100 < T < 150–200$ °C, Machel et al. 1995), the presence of which is confirmed by organic inclusions in sphalerite. Additional evidence for favorable temperatures for TSR are found in the isotopic results for 13 sphalerite-galena pairs, which yield consistent isotopic equilibration temperatures in the range 118–200 °C (Table 4).

The mean $\delta^{34}S$ values for sphalerite and galena, 9 and 6 ‰, respectively, are 6–9 ‰ lower than the average value for Triassic evaporites (15 ‰, Table 4). The offset is smaller than the kinetic isotope effect associated with TSR (−10 to −20 ‰; Machel et al. 1995), which implies that TSR consumed a substantial fraction of the available sulfate causing the isotope effect to be only partly preserved (Machel et al. 1995). Thermochemical reduction of younger marine sulfate would also be compatible with the data. For example, the isotopic offset of sphalerite and galena from marine sulfate of Miocene age ($\delta^{34}S \sim 22$ ‰; Paytan et al. 1998) would be 13–16 ‰, consistent with the full expression of the kinetic isotope effect.

The mean $\delta^{34}S$ value for barite (22 ‰) matches Miocene marine sulfate (~22 ‰) better than Triassic gypsum (~15 ‰, Table 4), but the Triassic sulfate is more likely to have been the source of barite sulfate. The supporting evidence can be seen in a plot of $\delta^{34}S$ versus $\delta^{18}O$ (Fig. 12c), which shows that the barite data extend toward the measured composition of Triassic gypsum rather than the composition of Miocene marine sulfate ($\delta^{34}S \sim 22$ ‰, $\delta^{18}O \sim 11$ ‰; Paytan et al. 1998; Turchyn and Schrag 2004). The colinearity of gypsum (Triassic sulfate) and barite strongly suggests that Triassic sulfate was the source of sulfate for barite formation and that the sulfate was isotopically modified by sulfate-consuming chemical reactions and possibly also by oxygen isotopic exchange reactions. Qualitatively, the isotopic modifications are what would be expected where TSR operated under conditions of limited sulfate supply, the increase in $\delta^{34}S$ reflecting the kinetically controlled preferential reduction of ^{34}S-depleted sulfate and the increase in $\delta^{18}O$ reflecting either preferential reduction of ^{18}O-depleted sulfate or thermally driven oxygen exchange between sulfate (or reduction intermediates) and H_2O. In that they show effects consistent with TSR under conditions of limited sulfate supply, the isotopic compositions suggest that barite may have formed from sulfate that remained at the site of ore formation after sphalerite and galena had precipitated. Thus, the simplest interpretation of the data is that Triassic evaporites furnished sulfur for both the sulfide and the barite event.

Processes of ore deposition

Sphalerite-galena stage At the temperatures of ore deposition in the diapiric zone of a carbonate-rich sequence, ore-forming concentrations of Zn and Pb are possible in a brine where the ratio of sulfate to reduced sulfur is very high. The deposition of the sphalerite-galena assemblage was most likely achieved by mixing this metal-bearing brine from deep in the basin with a reservoir of reduced sulfur already present in the diapir area. In this scenario, TSR processes involving organic matter in the diapir rocks had reduced sulfate in the diapir or in the fluids residing in the peridiapiric strata prior to the influx of the metalliferous brines. It is possible that TSR processes may have contributed to the reduced sulfur budget by in situ TSR of sulfate in the inbound metalliferous fluid by local organic matter. Mixing processes of a metal-rich brine with reduced sulfur not only precipitate sulfides but also generate large amounts of acid that must be buffered by the carbonate host rocks. This process is shown by the abundance of dissolution breccia and collapse-breccia, caves, and enhanced pore space, host rock replacements and extensive vuggy porosity in the host rocks. Cooling of the ore fluid, as suggested by the crystallization of fine-grained bipyramidal quartz, may have also contributed to the precipitation of sulfides, but to a lesser degree.

Barite stage The previous discussion of sulfur isotopes shows that the colinearity of sulfur isotopes for gypsum and barite strongly suggests that Triassic sulfate was the source of sulfate for barite formation and that the sulfate was isotopically modified by sulfate-consuming chemical reactions (i.e., TSR) and possibly also by oxygen isotopic exchange reactions. Therefore, barite deposition must have occurred when a Ba-rich fluid with low Zn, Pb and perhaps with highly reduced sulfur mixed with the sulfate brine in the area of the diapir. Acid is also produced in this reaction that also contributes to dissolution of the carbonate host rocks.

Fluorite stage (+minor Pb-Zn sulfide) The relatively high temperature of fluids responsible for fluorite deposition, and the dominance of a Na-rich fluid derived from the dissolution of halite are permissive for the formation of CaF-complexes. The high temperatures also account for the high metal contents measured in the fluid inclusions. At high temperatures, some reduced sulfur can be transported together with Zn and Pb (Yardley 2005). A fluid with this metal and fluorine load can deposit fluorite together with sphalerite and galena simply by cooling and fluid dilution.

Timing of mineralization, structural controls, tectonic triggers, and fluid migration

It is clear that multiple fluid reservoirs that include hydrocarbon-bearing fluids, evaporated seawater, halite dissolution brines as well as a presumed meteoric component were involved in the three distinct ore events at Bou Jaber. The interaction of these fluids with other fluids containing reduced sulfur (H_2S) or oxidized sulfur (SO_4^{2-}) was essential to precipitate sulfides and barite. Assuming the evaporated seawater component formed during the deposition of the Triassic evaporites, these very dense and low-viscosity brines probably migrated into the deep parts of the basin, including the Paleozoic basement rocks. Given that fluid mixing was likely an important depositional process, the ascent of the dense, deep basinal fluid into upper stratigraphic levels required exceptional hydrological events. Hydrological modeling of fluids in and about salt diapirs shows complex fluid regimes such as thermohaline and density convection, release of geopressured fluids and focusing of fluids along impermeable evaporites and diapiric structures (e.g., Kyle and Price 1986; Evan et al. 1991). In view of the complex fluid migration scenarios possible in diapiric environments, we suggest that normal basin- and diapir-controlled fluid migration mechanisms were not singularly responsible for the three mineral assemblages at Bou Jaber. If the Tunisian diapir-related ores formed from normal basin processes involving diapirs, then we would expect that there should be many more diapir-related ore deposits in the TSDP as well as in the Tethyan diapirs of central Algeria and western Morocco, as well as in Europe and other diapir provinces in the world.

There is an increasing appreciation that major sediment-hosted Zn-Pb ores formed as a result of large-scale tectonic triggers (Leach et al. 2010) that released deep-seated fluids into geochemical traps that precipitated the ores. This may be the situation for Bou Jaber and the other ore deposits of the TSDP. The first significant tectonic event after evaporite formation was mid-Cretaceous rifting during the Africa-Europe plate separation that produced tilted blocks, half-grabens, and salt diapirism. There is no evidence for ore emplacement during this tectonic and diapirism period. However, we suspect that the compressional events in mid-Eocene and in mid-Miocene related to the Africa-Europe plate subduction-collision during the Alpine orogeny that produced thrusting, SW–NE-trending folds and the return of salt diapirism may have been the tectonic trigger that brought deep-seated brines into the upper parts of the diapir body and into the peridiapiric cover rocks. The ascent of deep-seated Zn-Pb brines would have interacted with sources of reduced sulfur and hydrocarbons and precipitated the main-stage sphalerite and galena ores.

The diapirs may have focused fluid flow along the southeast flanks of the diapirs that define the Alpine thrusting. Diapir development was also responsible for the development of fracture permeability and creation of hydrocarbon and reduced sulfur chemical traps in the cover rocks. Furthermore, peak oil generation occurred in the Miocene and Pliocene (Belayouni 1992) during accelerated burial in parallel with the Alpine orogenic events. About 50 km south of Bou Jaber, the main oil fields produce hydrocarbons from the Serdj carbonate reservoir, similar to that hosting the Bou Jaber ores. Perhaps the reason for mineralization in some diapirs and not others could be the *quality* of the chemical traps or the involvement of some *special* steeply dipping deep-seated faults (perhaps the NW–SE faults that cut the NE–SW trend of the diapirs). The proposed migration of the deep-seated brines during the Alpine orogeny, related to the effects of Alpine collision, provided uplift of the basin and over-pressured fluids from thrust stacking and burial maturation of organic matter.

The previous discussion on deposition of the Zn-Pb rich ores proposed a fluid-mixing precipitation model that applies to many sediment-hosted Zn-Pb ores (e.g., Cooke et al. 2000; Leach et al. 2005). However, an enigmatic question is how do the barite and fluorite events connect to the Zn-Pb ores at Bou Jaber? Although Zn-Pb, barite and fluorite ores do occur together in some ore zones in Bou Jaber, this association is inconsistent within the deposit as well as in the region (few mineralized diapirs contain all three mineral assemblages). The three mineral assemblages are clearly geochemically and paragenetically distinct but yet they were controlled by the same diapiric structures related to the Alpine orogeny

during Eocene–Miocene time. As pointed out previously, the geochemical constraints on a hot basinal brine in a carbonate platform limits the ability of a single fluid to transport ore-grade amounts of Zn, Pb, Ba, and F. Consequently, we suggest that an evolving tectonic and structural regime during the Eocene–Miocene Alpine orogeny events resulted in the ascent of fluids from distinctly different fluid reservoirs. Zn-Pb rich ores formed by the mixing of an oxidized Zn-Pb brine into a hydrocarbon reservoir with reduced sulfur, barite formed by the mixing of a Ba-rich fluid with sulfate-rich fluids and meteoric water in the diapiric zone, and fluorite was deposited in the diapiric zone from a hot Na-rich brine by temperature decrease, dilution, and pH change in the diapiric zone.

The ore depositional events that produced the three distinct mineral assemblages may reflect the successive Alpine tectonic events during the middle Eocene to middle Miocene. During these events, transpressional tectonic stress developed the NW-trending grabens and related NW-trending faults that may have played an important role in ore formation. We suggest that the sulfides at Bou Jaber were deposited during the intense middle Eocene Alpine event that involved thrusting and halokinesis. Later barite mineralization may have occurred during the Oligocene Alpine event that resulted in the influx of meteoric water into Bou Jaber during the continental extensional environment. Finally, the fluorite ores may have overprinted the earlier mineralization during the middle Miocene folding, faulting, and thrusting event.

Exploration implications

Given the abundance of salt diapirs in the region, an obvious question is why do only a few have significant Zn-Pb mineralization? A likely factor that determines whether mineralization will occur in a diapir zone is the quality and size of the hydrocarbon and reduced sulfur reservoir. The essential role of a salt diapir in the mineralization process is the formation of a structural trap or reservoir around the diapir for hydrocarbon and reduced sulfur gases. The hydrocarbon and reduced sulfur-rich reservoir in the peridiapiric zone provides a chemical trap for ascending metalliferous brines. Factors that influence the quality of the trap are the abundance of gypsum/anhydrite in the mother salt, the size of the structural trap, and the permeability and porosity of the reservoir. The traps at Bou Jaber may have involved the diapir itself or the Late Albian Cenomanian shale Formation as the reservoir *seal* in the peridiapiric zone. Additionally, contacts between the Triassic evaporites and the shale-dominated Fahdene Formation (on both sides of the evaporite diapir) are potentially important traps that have not been recognized in the past.

The ores at Bou Jaber and other large tonnage deposits in the TSDP do not occur in the diapir itself, but are located in peridiapiric rocks containing quality hydrocarbon reservoirs. Mineralization is especially common at the NE and SW extremities of the salt structures. The locations of the ores appear to coincide with the possible intersections of the SW–NE deep basement faults with the NW-trending faults which define the Eocene–Miocene–Pliocene age NW-trending grabens. These intersecting fault zones may have been the vertical pathways for ascending metalliferous brines that precipitated ores in the peridiapiric zone. Therefore, the connectivity of faults in the basement with the upper diapiric zones must have been essential. Lacking the connectivity, a salt diapiric zone would remain sterile in sulfide mineralization.

A significant conclusion of the study provides evidence that decouples the mineral assemblages (Zn-Pb, fluorite and barite) into separate and genetically unrelated mineralization events. Consequently, the presence of barite or fluorite mineralization in any diapiric zone does not necessarily suggest the presence of Zn-Pb rich ores.

Conclusions

This paper provides new insights into the ore-forming environment, sources of the ore components and geological controls that produced the sphalerite, galena, barite, and fluorite ores of the Bou Jaber deposit. In contrast to previous authors, we show that the Zn-Pb, barite and fluorite mineral assemblages were produced by at least three separate and possibly unrelated mineralization events. The exact age(s) of the ores are uncertain. Field relations are consistent with mineral deposition during the multiple tectonic events of the Eocene–Miocene Alpine orogeny from multiple hydrothermal events: (1) Zn-Pb sulfides formed by mixing of two highly saline and high temperature fluids: one fluid metal-rich but reduced sulfur-poor and a second fluid containing reduced sulfur; (2) barite precipitation involved the influx of a meteoric water component that mixed with a barium-rich fluid; and (3) fluorite precipitated from a more saline fluid with higher temperatures.

Although the Bou Jaber ores are hosted in peridiapiric rocks, the fundamental genetic characteristics of the ore deposit are remarkably similar to those of the MVT family. There are no obvious connections to igneous events. The presence of abundant barite and fluorite with the Zn-Pb ores is unusual for a MVT deposit; however they overprinted a distinct and older Zn-Pb event. The Bou Jaber deposit can be classified as a MVT deposit, or as a MVT sub-type salt diapir-related deposit.

The deposition of Zn-Pb ores was controlled by the presence of a hydrocarbon-reduced sulfur reservoir in the peridiapiric environment. The endowment of Zn-Pb of the deposit was influenced by the quality of the trap, i.e., the abundance of gypsum/anhydrite in the mother salt, the size of the structural trap and the permeability and porosity of the

hydrocarbon-reduced sulfur reservoir which interacted with a metalliferous oxidized sedimentary brine. A deep-seated (basement?) fluid component must have had an efficient fluid pathway to ascend into the chemical sink in the peridiapiric zone. Therefore, the connectivity of faults in the basement with the upper diapiric zones was essential.

Acknowledgments We wish to thank Fethi M'Barek, director of the Bou Jaber mine, for his assistance to allow underground sampling. We wish also to thank Cyndi Kester, for assistance during the C, O, and S isotope analysis. The authors thank the following individuals for helpful discussions on the geology and halokinesis of the Tunisian Salt Diapir Province: Habib Belayouni, Saïd Tlig; Ali Zaier from the University of Tunis El Manar; Ahmed Braham from the Office National des Mines Tunisia and S.M.F. Sheppard from CRPG Nancy and ENS Lyon. Discussions with Pr. Habib Belayouni on the organic matter and mineralization relationships were very helpful. Karen Kelley from the USGS Denver and Bernd Lehman from Technical University of Clausthal are thanked for their constructive discussion and comments on the initial manuscript. Financial aid was provided to Salah Bouhlel by a research grant from the CIES/USA, Fulbright program.

References

Akrour H, Aoudjehane M, Othmanine A, Thibieoz J, Touahri B (1991) Gites et indices de fluorine de l'Algérie du Nord : Inventaire et réflexion. Bull Off Natl Géol Alger 2(1):11–28

Allan MM, Yardley BWD, Forbes LJ, Shmulovich KI, Banks DA, Shepherd TJ (2005) Validation of LA-ICP-MS fluid inclusion analysis with synthetic fluid inclusions. Am Mineral 90:1767–1775

Amouri M (1989) Les minéralisations Pb-Zn-Ba-F liées aux faciès carbonatés aptiens dans l'Atlas Tunisien Central. Géol Méditerr Marseille XVI(2–3):85–199

Banks DA, Giuliani G, Yardley BWD, Cheilletz A (2000) Emerald mineralization in Colombia: fluid chemistry and the role of brine mixing. Miner Deposita 35:699–713

Béjaoui J, Bouhlel S, Cardellach E, Canals A, Perona J, Piqué A (2013) Mineralization and fluid inclusion studies of the Aptian carbonate-hosted Pb-Zn-Ba ore deposits at Jbel Hamra, Central Tunisia. J Geochem Explor 128:136–146

Ben Ayed N (1986) Évolution tectonique de l'avant-pays de la chaîne alpine de Tunisie du début du Mésozoïque à l'Actuel. Thesis. University Paris Sud, Paris

Ben Ferjani F, Burrolet PF, Mejri F (1990) Petrolium Geology of Tunisia. Entreprise Tunisienne des Activités Pétrolière xx 1990

Belayouni H (1992) Oil seeps and associated phenomena in northern Tunisia. Field Trip guidebook, III^{ème} Journées de Géologie Tunisienne Appliquées à la Recherche des hydrocarbures ETAP Tunis pp 18

Belayouni H, Brunelli D, Clocchiatti R, Di Staso A, El Hassani I, Guerrera F, Kassaa S, Laridhi-Ouazaa N, Martín M, Serrano F, Tramontana M (2010) La Galite Archipelago (Tunisia, North Africa): Stratigraphic and petrographic revision and insights for geodynamic evolution of the Maghrebian Chain. J Afri Earth Sci 56(1):15–28

Belayouni H, Guerrera F, Martín MM, Serrano F (2012) Stratigraphic update of the Cenozoic Sub-Numidian formations of the Tunisian Tell (North Africa): Tectonic/sedimentary evolution and correlations along the Maghrebian Chain. J Afr Earth Sci 64:48–64

Bellon H (1976) Séries magmatiques néogènes et quaternaires du pourtour de la Méditerranée occidentale, comparées dans leur cadre géochronologique; implications géodynamiques. Thèse Etat Orsay

Bodnar RJ (1993) Revised equation and table for determining the freezing-point depression of H_2O-NaCl solutions. Geochim Cosmochim Acta 57:683–684

Boltenhagen C (1985) Paléogéographie du crétacé moyen de la Tunisie centrale. 1er Congr Nat Sci Terre 1:97–114

Bolze J (1954) Ascension et percée de diapirs au Crétacé moyen dans les monts de Téborsouk. C R Somm Soc Géol Fr 7:139–141

Bolze J, Burollet PF, Castany G (1952) Le sillon tunisien, Monographies régionales, XIXe Congrès Géologique International, Alger, 2e série, *n*° 5, pp 112

Bouabdellah M, Brown AC, Sangster DF (1996) Mechanisms of formation of internal sediments at the Beddiane lead-zinc deposit, Toussit mining district, northeastern Morocco. Econ Geol Spec Publ 4:356–363

Bouabdellah M, Castorina F, Bodnar RJ, Banks D, Jébrak M, Prochaska W, Lowry D, Klügel A, Hoemle M (2013) Petroleum migration, fluid mixing, and halokinesis as the main ore-forming processes at the peridiapiric Jbel Tirremi fluorite-barite hydrothermal deposit, northeastern Morocco. Econ Geol 109:1223–1256

Bouaziz S, Barrier E, Soussi M, Turki MM, Zouari H (2002) Tectonic evolution of the northern African margin in Tunisia from paleostress data and sedimentary record. Tectonophysics 357:227–253

Bouhlel S (1982) Distribution du baryum et du strontium dans la province fluorée tunisienne; application aux gîtes de Hammam Jédidi et Hammam Zriba-Jebel Guebli. PhD Thesis, University of Toulouse III, France

Bouhlel S (1985) Composition chimique, fréquence des minéraux de la série barytine-célestite dans les gisements de fluorine de Hammam Jédidi et Hammam Zriba-Jebel Guebli (Tunisie Nord-Orientale). Bull Mineral 108:403–420

Bouhlel S (1987) Mineralized carbonates in fluorite and Pb-Zn ore deposits: Jurassic and Upper Cretaceous of northern Tunisia. In: Excursion Guidebook I.A.S. 8th Regional Meeting of Sedimentology, pp 1–44

Bouhlel S (1993) Gîtologie, minéralogie et essai modélisation des minéralisations à F-Ba-Sr-Pb-Zn-(S°) associées aux carbonates (jurassiques et crétacés) et aux diapirs triasiques : gisements de Stah-Kohol, Zriba, Guebli, Bou Jaber et Fedj el Adoum (Tunisie septentrionale). Thèse Doctorat d'Etat, University of Tunis El Manar, Tunisia

Bouhlel S (2005) Carbonate-hosted Mississippi Valley-type Pb-Zn deposits in Tunisia (eastern Atlassic Foreland belt). In: Zhao C and Guo B (eds) Mineral deposits research—Meeting the global challenge. Proceedings of the Eighth Biennial SGA Meeting (Beijing, China) 3:19–22

Bouhlel S, Fortuné JP, Guilhaumou N, Touray JC (1988) Les minéralisations stratiformes à F-Ba de Hammam Zriba, Jebel Guebli (Tunisie Nord Orientale): l'apport des études d'inclusions fluides à la modélisation génétique. Miner Deposita 23:166–173

Bouhlel S, Johnson CA, Leach DL (2007) The peridiapiric-type Pb-Zn deposit at Fedj el Adoum, Tunisia: geology, petrography, and stable isotopes. In: Andrew CJ et al. (eds) Proc Ninth Biennial SGA Meeting (Dublin, Ireland) 1:323–326

Bouhlel S, Leach DL, Johnson CA, Lehmann B (2009) Ore textures and isotope signatures of the peridiapiric carbonate-hosted Pb-Zn deposit of Bou Grine, Tunisia. In Smart Science for Exploration and Mining P. J. Williams et al. (eds) Proceedings of the Tenth Biennial SGA Meeting (Townsville, Australia) 1:409–411

Bouhlel S, Garnit H, Béjaoui J, Skaggs S (2013) Lead isotopes signatures of the MVT lead-zinc (±F) deposits across Central-North Tunisia: evidence for the heterogeneity in uranium component of the underlying source rocks. In: Mineral deposit research for a high-tech

world. Jonsson E et al. (eds) Proceedings of the 12th Biennial SGA Meeting (Uppsala, Sweden) 2:612–615

Bouzenoune A, Lécolle P (1997) Petrographic and geochemical arguments for hydrothermal formation of the Ouenza siderite deposit (NE Algeria). Miner Deposita 32:189–196

Braham A, Hatira N, Hammami M, Kadri A, Arfaoui M, Chihi L, Mansouri A, Souid R (2002) Le diapir de Bou Jaber (Tunisie Centre Ouest) Précisions biostratigraphiques et conséquences structurales. Serv Géol Tunisie 69:93–103

Burke WH, Denison RE, Hetherington EA, Keopnick RB, Nelson HF, Otto JB (1982) Variation of seawater $^{87}8r/^{86}Sr$ throughout Phanerozoic time. Geology 10:516–519

Burollet PF (1956) Contribution à l'étude stratigraphique de la Tunisie centrale. Ann Min Géol (Tunis) No.18

Calvez JY, Orgeval JJ, Marcoux E (1986) Étude isotopique du plomb du gisement de Bou Grine (Zone des dômes, Tunisie) et comparaison avec quelques données de la province tunisienne. BRGM Sci Tech 121–123

CastanyG (1952) Paléogéographie, tectonique et orogenèse de la Tunisie. XIXth international Geological Congress, "Monographies Régionales", 2 (1) pp 63

Chaari (2002) Geochemical study of Late Albian and Cenomanian-Turonian source rocks: a key to assess the geodynamic evolution of petroleum system of Jebel Goraa area, Salt dome zone, Northern Tunisia. Master thesis, University Tunis el manar, Faculty of Sciences of Tunis

Charef A, Sheppard SMF (1987) Pb-Zn mineralization associated with diapirism: fluid inclusion and stable isotope (H, C, O) evidence for the origin and evolution of the fluids at Fedj-el-Adoum, Tunisia. Chem Geol 61:113–134

Chihi L (1995) Les fossés néogènes à quaternaires de la Tunisie et de la mer pélagienne: leur étude structurale et leur signification dans le cadre géodynamique de la méditerranée centrale, Thesis. University of Tunis El Manar, Tunisia

Claypool GE, Molsen WT, Kaplan IR, Sakai M, Zak I (1980) The age of curves of sulfur and oxygen isotopes in marine sulfate and their mutual interpretation. Chem Geol 28:199–260

Cooke DR, Bull SW, Large RR, McGoldrick PJ (2000) The importance of oxidized brines for the formation of Australian Proterozoic stratiform sediment-hosted Pb-Zn (Sedex) deposits. Econ Geol 95:1–18

Decrée S (2008) Caractérisation géochimique et isotopique dans un système d'altération complexe du protolithe magmatique à la minéralisation fer-plomb-zinc : le cas de la mine de Sidi Driss. Thesis, Université Libre de Bruxelles

Decrée S, Marignac C, De Putter T, Deloule E, Liégeois JP, Demaiffe D (2008) Pb-Zn mineralization in a Miocene regional extensional context: the case of the Sidi Driss and the Douahria ore deposits (Nefza mining district, northern Tunisia). Ore Geol Rev 34:285–303

Dewey JF, Helman ML, Turco E, Hutton, Knott SD (1989) Kinematics of the western Mediterranean. In : Alpine Tectonics, Coward MP, DietrichD and Parker G (eds), Geological Society Special Publication 45:265–283

Dubourdieu G (1956) Étude géologique de la région de l'Ouenza (confins algéro-tunisiens). Serv Carte Géol Algérie Alger No. 10

Evan DG, Nunn JA, Hanor JS (1991) Mechanisms of driving groundwater flow near salt domes. Geophysical Reasearch 94:927–930

Erraoui L (1994) Environnements sédimentaires et géochimie des séries de l'Eocène du Nord-Est de la Tunisie. Thèse de Doctorat de Spécialité. University of Tunis El Manar, Tunisia

Frank MH, Lohmann KC (1986) Textural and chemical alteration of dolomite: Interaction of mineralizing fluids and host rock in a Mississippi Valley-type deposit, Bonneterre Formation, Viburnum Trend. In: Hagni RD (eds) Process mineralogy VI: Warrendale PA Metallurgical Society 103–116

Fuchs Y (1973) Sur les relations entre émersion et concentration métallifére (quelques exemples tunisiens). In: Livre Jubilaire Solignac. Ann Mines Géol Tunis 26:479–509

Garnit H, Bouhlel S, Barca D, Craig AJ, Chtara C (2012) Phosphorite-hosted zinc and lead mineralization in the Sekarna deposit (Central Tunisia). Miner Deposita 47:546–562

Giesemann A, Jager HJ, Norman AL, Krouse HR, Brand WA (1994) On-line sulfur determination using an elemental analyser coupled to a mass spectrometer. Anal Chem 66:2816–2819

Goldstein RH, Reynolds TJ (1994) Systematics of fluid inclusions in diagenetic minerals. SEPM Short Course 31:1–199

Grandia F, Canals À, Cardellach E, Banks DA, Perona J (2003) Origin of ore-forming brines in sediment-hosted Zn-Pb deposits of the Basque-Cantabrian basin, northern Spain. Econ Geol 98:1397–1411

Guilhaumou N, Szydlowski N, Pradier B (1990) Characterization of hydrocarbon fluid inclusions by infra-red and fluorescence microspectrometry. Min Mag 54:311–324

Guillong M, Meir DL, Allan MM, Heinrich CA, Yardley BWD (2008) SILLS: A Matlab based program for the reduction of Laser Ablation ICP-MS data of homogeneous materials and inclusions. Miner Assoc Can Short Course 40:328–333

Guirand R, Maurin JC (1991) Le rifting en Afrique au Crétacé inférieur: synthèse structurale, mise en évidence de deux étapes dans la génèse des bassins, relation avec les ouvertures océaniques peri-africaines. Bull Soc Geol Fr 162(5):811–823

Hanna MA, Wolf A (1934) Texas and Louisiana salt dome cap rock minerals. Bull Am Assoc Petr Geol 3:212–225

Jrad L, Perthuisot V (1995) Diapirisme, orogenèse et mineralisation Pb-Zn en Afrique du Nord: exemple des gisements du J. Ajred et du J. Hamra en Tunisie centrale. C R Acad Sci Paris 321:721–728

Juteau M, Michard A, Albared F (1986) The Pb-Sr-Nd isotope geochemistry of some recent circum-Mediterranean granites. Contrib Mineral Petrol 92:331–340

Kampschulte A, Strauss H (2004) The sulfur isotopic evolution of Phanerozoic seawater based on the analysis of structurally substituted sulfate in carbonates. Chem Geol 204:255–286

Kendrick MA, Burgess R, Leach D, Patrick RAD (2002) Hydrothermal fluid origins in Mississippi Valley-type ore deposits: combined noble gas (He, Ar, Kr) and halogen (Cl, Br, I) analysis of fluid inclusions from the Illinois-Kentucky fluorspar district, Viburnum trend, and the Tri-State districts, Midcontinent United States. Econ Geol 97:453–469

Koepenick RB, Burke WH, Denison RE, Hetherington EA, Nelson HF, Otto JB, Waite LE (1985) Construction of the seawater $^{87}Sr/^{86}Sr$ curve for the Cenozoic and Cretaceous: supporting data. Chem Geol 58(1–2):55–81

Kyle JR, Posey HH (1991) Halokinesis, cap rock development and salt dome mineral resources. In: Melvin JL (eds) Evaporites Petroleum and Mineral Resources: Developments in Sedimentology 50: 413–474

Kyle JR, Price PK (1986) Metallic sulphide mineralization in salt-dome cap rocks, Gulf Coast, U.S.A. Trans Inst Min Metall Sect B 95:B6–B16

Land LS (1980) The isotopic chemistry and trace element geochemistry of dolomite: the state of the art. SEPM 28:87–110

Lange S, Chaudhuri S, Clauer N (1983) Strontium isotopic evidence for the origin of barites and sulfides from the Mississippi Valley-type ore deposits in southeast Missouri. Econ Geol 78(6):1255–1261

Laridhi-Ouazaa N (1994) Étude minéralogique et géochimique des episodes magmatiques mesozoiques et miocènes de la Tunisie, Thesis. University of Tunis El Manar, Tunisia

Leach DL, Sangster DF (1993) Mississippi Valley-type lead-zinc deposits. In: Kirkham RV, Sinclair WD, Thorp RI, Duke JM (eds) Mineral Deposit Modelling Geol Ass Canada Spec Paper 40: 289–314

Leach DL, Sangster DF, Kelly KD, Large RR, Carven G, Allen CR, Gutzmen J, Walters S (2005) Sediment- hosted lead-zinc deposits: a global perspective. In: Hedenquist JW, Thompson JFH, Goldfarb RJ, Richards JP (eds) Econ Geol 100th Anniv Vol, pp 561–607

Leach DL, Taylor RD, Fey DL, Diehl SF, Saltus RW (2010) A deposit model for Mississippi Valley-type lead-zinc ores. In: Mineral deposit models for resource assessment. http://www.usgs.gov/ pubprod.

Leach DL, Song YC, Hou ZQ, Yang TA, Xue CD (2013)The giant Jinding Zn-Pb deposit: Ore formation in an evaporitedome, Lanping Basin, Yunan, China. In: Mineral deposit research for a high-tech world. Jonsson E et al. (eds) Proceedings of the 12th Biennial SGA Meeting (Uppsala, Sweden) 3:1424–1427

Light MPR, Posey HH, Kyle JR, Price PE (1987) Model for the origins of geopressured brines, hydrocarbons, cap rocks and metallic mineral deposits: Gulf Coast, U.S.A. In: Lerche L, O'Brien J (eds) Dynamical Geology of Salt and Related Structures, Academic Press, pp. 497–542

M'Rabet A (1987) Stratigraphie, sédimentation et diagenèse carbonatée des séries du Crétacé inférieur de la Tunisie centrale. Ann Mines Géol Tunis 30:412

Maameri K, Daadouch Imed (1986) Etude des indices de pétrole en surface dans la Tunisie des avant nappes. Mémoire de Fin d'Etude Ingénieur, Faculté des Sciences de Tunis, Université Tunis el Manar

Machel HG, Krouse HR, Sassen R (1995) Products and distinguishing criteria of bacterial and thermochemical sulfate reduction. Appl Geochem 10:373–389

Macquar JC, Rouvier H, Thibiéroz J (1990) Les minéralisations Zn, Pb, Fe, Ba, F péri-cévenoles: cadre structuro-sédimentaire et distribution spatio-temporelle. Doc BRGM Orléans 183:143–158

Marie J, Trouve P, Desforges G, Dufaure P (1984) Nouveaux éléments de paléogéographie du Crétacé de Tunisie. Notes Mém TOTAL-CFP Paris 19:37

Martinez C, Truillet R (1987) Evolution structurale et paléogeographie de la Tunisie. Mem Soc Geol It 38:35–45

Masse JP, Chikhi-Aouimer F (1982) La plate-forme carbonatée de l'Ouenza (Sud canstantinois-Algerie) Organisation et dynamique Durant l'Aptian supérieur. Géol Mediterr IX(3):259–267

Matlock JF, Misra KC (1993) Sphalerite-bearing detrital 'sand' bodies in Mississippi Valley-type zinc deposits, Mascot-Jefferson City district, Tennessee Implications for the age of mineralization. Mineral Deposita 28:344–353

Mc Limans RK (1975) Systematic fluid inclusion and sulfide isotope studies of the Upper Mississippi Valley Pb-Zn deposits. Econ Geol 70(7):1324, **Abstract**

Mc Limans RK (1977) Geological, fluid inclusion, and stable isotope studies of the Upper Mississippi Valley zinc-lead district, southwest Wisconsin: Ph.D. thesis, Pennsylvania State University

McCrea JM (1950) On the isotopic chemistry of carbonates and a paleotemperature scale. J Chem Phys 18:849–857

Mejri F, Burollet PF, Ben Ferjani A (2006) Petroleum Geology of Tunisia, A Renewed Synthesis.Entreprise Tunisienne des Activités Pétrolières, Tunis. Memoir No. 22pp 233

Nesbitt BE, Muehlenbachs K (1994) Paleohydrogeology of the Canadian Rockies and origins of basinal brines, Pb-Zn deposits and dolomitization in the Western Canada sedimentary basin. Geology 22:243–246

Orgeval JJ (1994) Peridiapiric metal concentrations: example of the Bou Grine deposit (Tunisian Atlas). In: Fontboté L, Boni M (eds) Sediment-hosted Zn-Pb ores. Society for Geology Applied to Mineral Deposits Spec Publ 10:354–389

Paytan A, Kastner M, Campbell D, Thiemens MH (1998) Sulfur isotopic composition of Cenozoic seawater sulfate. Science 282:1459–1462

Perthuisot *V* (1978) Dynamique et pétrogenèse des extrusions triasiques en Tunisie septentrionale. Thesis, École Normale Sup Paris

Perthuisot V (1981) Diapirism in northern Tunisia. J Struct Geol 3:231–235

Perthuisot V, Rouvier H (1992) Les diapirs d'Algerie et de Tunisie : des appareils varies, resultats d'une evolution structurale et petrogenetique complexe. Bull Soc Géol Fr 163(6):751–760

Perthuisot V, Rouvier H, Smati A (1998) Style et importance des déformations anté-vraconiennes dans le Maghreb oriental: exemple du diapir du Jebel Slata. Bull Soc Géol Fr 8:389–398

Philip H, Andrieux J, Dlala M, Chihi L, Ben Ayed N (1986) Evolution tectonique mio-plio-quaternaire du Fossé de Kasserine (Tunisie centrale); implications sur l'évolution géodynamique récente de la Tunisie. Bull Soc Géol Fr 2(8):559–568, **No.5-6**

Plumlee GS, Leach DL, Hofstra AH, Landis GP, Rowan EL, Viets JG (1994) Chemical reaction path modeling of ore deposition in Mississippi Valley-type Pb-Zn deposits of the Ozark region, US Midcontinent. Econ Geol 89:1361–1383

Posey HH, Kyle JR (1988) Fluid-rock interactions in the salt dome environment: an introduction and review. Chem Geol 74:1–24

Posey HH, Kyle JR, Agee WN (1994) Relations between diapiric salt structures and metal concentrations, Gulf Coast sedimentary basin, Southern North America. In: Fontboté L, Boni M (eds) Sediment hosted Zn-Pb ores. Society for Geology Applied to Mineral Deposits Spec Publ 10:140–164

Price PE, Kyle JR (1983) Metallic sulphide deposits in Gulf Coast salt-dome caprocks. Gulf Coast Assoc Geol Soc Trans 33:189–193

Roedder E (1963) Studies of fluid inclusions, II: freezing data and their interpretation. Econ Geol 58:167–211

Roedder E (1984) Fluid inclusions. Rev Mineral Am Mineral Soc 12:646

Rouvier H (1977) Géologie de l'Extrême-Nord tunisien: tectonique et paléogéographie superposées à l'extrémité de la chaîne nord-maghrébine. Ann Mines Géol Tunis 29:427

Rouvier R, Perthuisot V, Mansouri A (1985) Pb-Zn deposits and salt bearing diapirs in southern Europe and North Africa. Econ Geol 80:666–687

Saïdi M, Belayouni H (1994)Étude géologique et géochimique des roches mères albo-vraconienne dans le domaine de la Tunisie centro-septentrional. Proceeding of the 4th Petroleum Exploration Conference 7:91–116, Tunis

Sainfeld P (1956) The lead-zinc-bearing deposits of Tunisia. Econ Geol 51:150–177

Salmi-Laouar S (2004) Contribution à l'étude géologique et géochimie des isotopes stables (S,0, C) des minéralisation polymétallique (Zn, Pb, F, Ba, Fe) de la zone des diapirs du nord de Tébessa, NE Algerien) Thèse de Doctorat d'Etat. Université de Annaba, Algerie

Salmi-Laouar S, Laouar R, Boyce AJ, Boutaleb A, Zerdazi A, Arouch YE (2004) Rapports istotopiques du soufre, de l'oxygène et du carbone dans le massif de Bou Jaber, NE algerien: Origine des minéralisations à Pb-Zn-Ba et sources des fluides. Serv Géol Algérie 15:3–25

Salmi-Laouar S, Laouar R, Boyce AJ, Boutaleb A, Lamouroux C (2007) Premières données isotopiques sur la mer triasique dans l'Atlas Saharien Oriental (Algérie). Serv Géol Algérie 18:315–323

Sass-Gustkiewics M (1996) Internal sediments as a key to understanding the hydrothermal karst origin of the Upper Silesia Zn-Pb ore deposits. Econ Geol Spec Publ 4:171–181

Schmidt SC (1999) Re-activation of the Bougrine Mine, Tunisia. 101st Ann Gen Meeting, Can Inst Min Metal Petro, Techn Progr CD-ROM : Major Canadian Overseas Project Paper 1:1–9

Sheppard SMF, Charef A, Bouhlel S (1996) Diapirs and Zn-Pb mineralizations: a general model based on Tunisian (N. Africa) and Gulf Coast (U.S.A.) deposits. Econ Geol Spec Publ 4:230–243

Skaggs S, Norman N, Garrison E, Coleman D, Bouhlel S (2012) Local mining or lead importation in the Roman province of Africa Proconsularis? Lead isotope analysis of curse tablets from Roman Carthage, Tunisia. J Archaeol Sci 39(4):970–983

Soua M (2009) Structural context of the paleogeography of the Cenomanian-Turonian anoxic event in the eastern Atlas basins of the Maghreb. CR Geosci 341(12):1029–1037

Spangenberg J, Fontboté L, Sharp ZD, Hunziker J (1996) Carbon and oxygen isotope study of hydrothermal carbonates in the zinc-lead deposits of the San Vicente district, central Peru. Chem Geol 133: 289–315

Tlig S, Erraioui L, Ben Aissa L, Aluoani R, Tagorti MA (1991) Tectogenèses alpine et atlasique : deux événements distincts dans l'histoire géologique de la Tunisie. Corrélation avec les événements clés en Méditerranée. Comptes Rendus de l'Académ de Sci Paris 312(Série II):295–301

Tlig S, Sahli H, Er-Raioui L, Alouani R, Mzoughi M (2010) Depositional environment controls on petroleum potential of the Eocene in the North of Tunisia. J Pet Sci Eng 71(3–4):91–105

Turchyn AV, Schrag DP (2004) Oxygen isotope constraints on the sulfur cycle over the past 10 million years. Science 303:2004–2007

Turki MM, Delteil J, Truillet R, Yaich C (1988) Les inversions tectoniques de la Tunisie centro-septentrionale. Bull Soc Géol France (8) IV 3:399–406

Ulrich MR, Bodnar RJ (1988) Systematic stretching of fluid inclusions. II. Barite at 1 atmosphere confining pressure. Econ Geol 83: 1037–1046

Veizer J, Compston W (1974) $^{87}Sr/^{86}Sr$ composition of seawater during Phanerozoic. Geochim Cosmochim Acta 38:1461–1484

Veizer J, Hoefs J (1976) The nature of O-18 /O-16 and C-13 /C-12 secular trends in sedimentary carbonate rocks. Geochim Cosmochim Acta 40(11):1387–1395

Vially R, Letouzey J, Bernard F, Haddadi N, Deforges G, Askri H, Boudjema A (1994) Basin inversion along the North African margin: the Sahara Atlas (Algeria). In: Roure F (ed) PeriTethyan platforms. Technip, Paris, pp 79–118

Vila JM, Charrière A (1993) Découverte d'Albien calcaire et de Trias resédimenté au Djebel Bou Jaber (partie ouest, Algérie); corrélations avec les forages et conséquences sur l'organisation du Crétacé inférieur des confins algéro-tunisiens. C R Acad Sci 316(2): 243–249

Vila J-M, Ben Youssef M, Bouhlel S, Ghanmi M, Kassaâ S, Miaadi F (1998) Tectonique en radeaux au toit d'un glacier de sel sous-marin albien de Tunisie du Nord-Ouest : exemple du secteur minier de Gueurn Halfaya. C R Acad Sci Paris 327:563–570

Vila JM, Kassaâ S, Bouhlel S, Ben Youssef M, Dali T, Ghanmi M (1999) Inversion tectonique de structures halocinétiques et localisation des minéralisations (Zn, Sr): émergence au Jebel Bou Khil (Nord-Ouest tunisien) d'un chevauchement entre un domaine nord à « glaciers de sel » sous-marins et un domaine sud à « diapirs typiques ». Bull Soc Géol Fr 170(2):161–172

Xue C, Zeng R, Liu S, Chi G, Qing H, Chen Y, Yang J, Wang D (2007) Geologic, fluid inclusion and isotopic characteristics of the Jinding Zn–Pb deposit, western Yunnan, South China: a review. Ore Geol Rev 31:337–359

Yardley BWD (2005) 100th Anniversary Special Paper: metal concentrations in crustal fluids and their relationship to ore formation. Econ Geol 100:613–632

Zartman RE, Doe BR (1981) Plumbotectonics—the model. Tectonophysics 75:135–162